


A cascade of magmatic events during the assembly and eruption of a super-sized magma body

Aidan. S. R. Allan¹ · Simon J. Barker^{1,2} · Marc-Alban Millet^{1,3} · Daniel J. Morgan⁴ · Shane M. Rooyackers^{1,5} · C. Ian Schipper¹ · Colin J. N. Wilson¹ 

Received: 10 October 2016 / Accepted: 8 May 2017 / Published online: 5 June 2017
© Springer-Verlag Berlin Heidelberg 2017

Abstract We use comprehensive geochemical and petrological records from whole-rock samples, crystals, matrix glasses and melt inclusions to derive an integrated picture of the generation, accumulation and evacuation of 530 km³ of crystal-poor rhyolite in the 25.4 ka Oruanui supereruption (New Zealand). New data from plagioclase, orthopyroxene, amphibole, quartz, Fe–Ti oxides, matrix glasses, and plagioclase- and quartz-hosted melt inclusions, in samples spanning different phases of the eruption, are integrated with existing data to build a history of the magma system prior to and during eruption. A thermally and compositionally zoned, parental crystal-rich (mush) body was developed during two periods of intensive crystallisation, 70 and 10–15 kyr before the eruption. The mush top was quartz-bearing and as shallow as ~3.5 km deep, and

the roots quartz-free and extending to >10 km depth. Less than 600 year prior to the eruption, extraction of large volumes of ~840 °C low-silica rhyolite melt with some crystal cargo (between 1 and 10%), began from this mush to form a melt-dominant (eruptible) body that eventually extended from 3.5 to 6 km depth. Crystals from all levels of the mush were entrained into the eruptible magma, as seen in mineral zonation and amphibole model pressures. Rapid translation of crystals from the mush to the eruptible magma is reflected in textural and compositional diversity in crystal cores and melt inclusion compositions, versus uniformity in the outermost rims. Prior to eruption the assembled eruptible magma body was not thermally or compositionally zoned and at temperatures of ~790 °C, reflecting rapid cooling from the ~840 °C low-silica rhyolite feedstock magma. A subordinate but significant volume (3–5 km³) of contrasting tholeiitic and calc-alkaline mafic material was co-erupted with the dominant rhyolite. These mafic clasts host crystals with compositions which demonstrate that there was some limited pre-eruptive physical interaction of mafic magmas with the mush and melt-dominant body. However, the mafic magmas do not appear to have triggered the eruption or controlled magmatic temperatures in the erupted rhyolite. Integration of textural and compositional data from all available crystal types, across all dominant and subordinate magmatic components, allow the history of the Oruanui magma body to be reconstructed over a wide range of temporal scales using multiple techniques. This history spans the tens of millennia required to grow the parental magma system (U–Th disequilibrium dating in zircon), through the centuries and decades required to assemble the eruptible magma body (textural and diffusion modelling in orthopyroxene), to the months, days, hours and minutes over which individual phases of the eruption occurred, identified through field observations

Communicated by Gordon Moore.

Electronic supplementary material The online version of this article (doi:[10.1007/s00410-017-1367-8](https://doi.org/10.1007/s00410-017-1367-8)) contains supplementary material, which is available to authorized users.

✉ Colin J. N. Wilson
colin.wilson@vuw.ac.nz

- ¹ School of Geography, Environment and Earth Sciences, Victoria University of Wellington, P.O. Box 600, Wellington 6140, New Zealand
- ² School of Environment, University of Auckland, PB92019, Auckland 1142, New Zealand
- ³ School of Earth and Ocean Sciences, Cardiff University, Cardiff CF10 3AT, UK
- ⁴ School of Earth and Environment, University of Leeds, Leeds LS2 9JT, UK
- ⁵ Department of Earth and Planetary Sciences, McGill University, Montreal, QC H3A 0E8, Canada

tied to diffusion modelling in magnetite, olivine, quartz and feldspar. Tectonic processes, rather than any inherent characteristics of the magmatic system, were a principal factor acting to drive the rapid accumulation of magma and control its release episodically during the eruption. This work highlights the richness of information that can be gained by integrating multiple lines of petrologic evidence into a holistic timeline of field-verifiable processes.

Keywords Oruanui eruption · Taupo volcano · Rhyolite · Magma chamber · Magma accumulation · Eruption timings

Introduction

The nature and generation of large silicic magma bodies

The study of large silicic eruptions and their parental magmatic systems offers many challenges. One central issue is determining whether the processes and timescales involved in the generation of small volumes of evolved magma are the same as for the accumulation of vast magma bodies that feed supereruptions (i.e. $>10^{15}$ kg or ~ 450 km³ magma; e.g. Self 2006). Do large bodies of eruptible magma take longer to be generated than smaller ones (e.g. Smith 1979; Shaw 1985; Reid 2008; de Silva and Gregg 2014), or do they accumulate on similar timescales, driven by processes with faster rates (e.g. Wilson and Charlier 2009; Gualda et al. 2012a; Wotzlaw et al. 2015)? By extension, questions arise as to how such vast volumes of melt-rich magma can accumulate without erupting, what controls the lifetime of eruptible magma bodies and what triggers eruption onset (e.g. Gregg et al. 2012; Gelman et al. 2013; Caricchi et al. 2014a; Malfait et al. 2014; Myers et al. 2016)?

Answers to these questions are sought either by numerical modelling (e.g. Jellinek and DePaolo 2003; Bachmann and Bergantz 2004; Huber et al. 2011, 2012) or geochemical and petrological investigation of eruption products (e.g. Girard and Stix 2010; Gualda et al. 2012a); the latter approach having the advantage of directly linking to hard evidence in the field (e.g. Wilson et al. 2006; Wilson and Charlier 2009; Allan et al. 2012, 2013; Bain et al. 2013). Petrological studies can be controversial (particularly in the case of the Bishop Tuff), as it is essential to interpretations of petrological data to determine if crystals grew together in situ over a definable range of intensive variables (Hildreth 1979; Gualda et al. 2012a, b; Evans and Bachmann 2013; Chamberlain et al. 2015), or if they are aggregated from a wide range of sources (e.g. Eichelberger 1978; Gamble et al. 1999; Dungan and Davidson 2004; Davidson et al. 2005). Furthermore, it is desirable for multiple co-erupted crystal phases to be considered together (e.g. Hildreth

1979; Girard and Stix 2010; Chamberlain et al. 2014a, 2015). Although useful information can be recovered from studies of single phases (e.g. Bishop Tuff quartz—Peppard et al. 2001; Wark et al. 2007; Thomas et al. 2010; Gualda et al. 2012a, Pamukcu et al. 2012, 2016; Gualda and Sutton 2016) there is a risk of introducing unintended systematic bias.

The crystal archive in crystal-poor ignimbrites

The crystal mush model (e.g. Brophy 1991; Hildreth 2004; Bachmann and Bergantz 2004, 2008; Bachmann and Huber 2016) provides a widely utilised framework with which to explore large crustal bodies of silicic magma. The mush itself has generally been envisaged as a largely un-eruptible body of viscous material (Smith 1979), and numerical modelling has focussed on determining how mush bodies might ‘defrost’ and/or remobilise (Burgisser and Bergantz 2011; Huber et al. 2010, 2011). Mafic magma is often implicated in supplying the heat and volatiles required to mobilise the mush to drive voluminous eruptions of crystal-rich magma (e.g. Parmigiani et al. 2014). However, the origins and rates of accumulation of crystal-poor rhyolites, which are generally thought have been extracted from mush zones, are potentially widely diverse (Bachmann and Bergantz 2008; Bachmann and Huber 2016 for overviews).

Two considerations from the crystal mush model pertain to the origins of crystal-poor rhyolites. (1) Large volumes of evolved melt may be available for extraction from a mush zone at any given point in time. (2) If crystal-poor rhyolite does originate from a crystal-rich reservoir, crystal-melt segregation on a massive scale is required at some stage prior to eruption. It is not yet known if such large-scale segregation leaves a tangible record of this process in the small fraction of crystals that are actually erupted and, if so, how such records could be used to temporally and physically constrain these events. A further complication is that any signals recorded in crystals of events related to melt body generation must be deconvoluted from subsequent growth in the eruptible magma. This last point raises questions of which crystals are phenocrystic (grown in the melt with which they were erupted), antecrystic (derived from consanguineous parental sources), or xenocrystic (foreign to the magma in which they are found) (Bacon and Lowenstern 2005; Charlier et al. 2005). It is also possible that a given crystal may contain domains attributable to all three origins (e.g. Charlier et al. 2008).

In this paper we document the timing and mechanisms of pre- and syn-eruptive magmatic processes for the Oruanui eruption (Taupo, New Zealand). We integrate new and published major- and trace-element analyses of whole-rock samples, matrix glasses, crystals, and quartz- and plagioclase-hosted melt inclusions (see Table S.1), for both the

volumetrically dominant rhyolites and subordinate co-erupted mafic magmas. We explore the textural and compositional relationships within and between crystal phases, to provide a summary of the magmatic processes and their associated timescales that operated during the establishment, assembly and eruption of the super-sized Oruanui magma body.

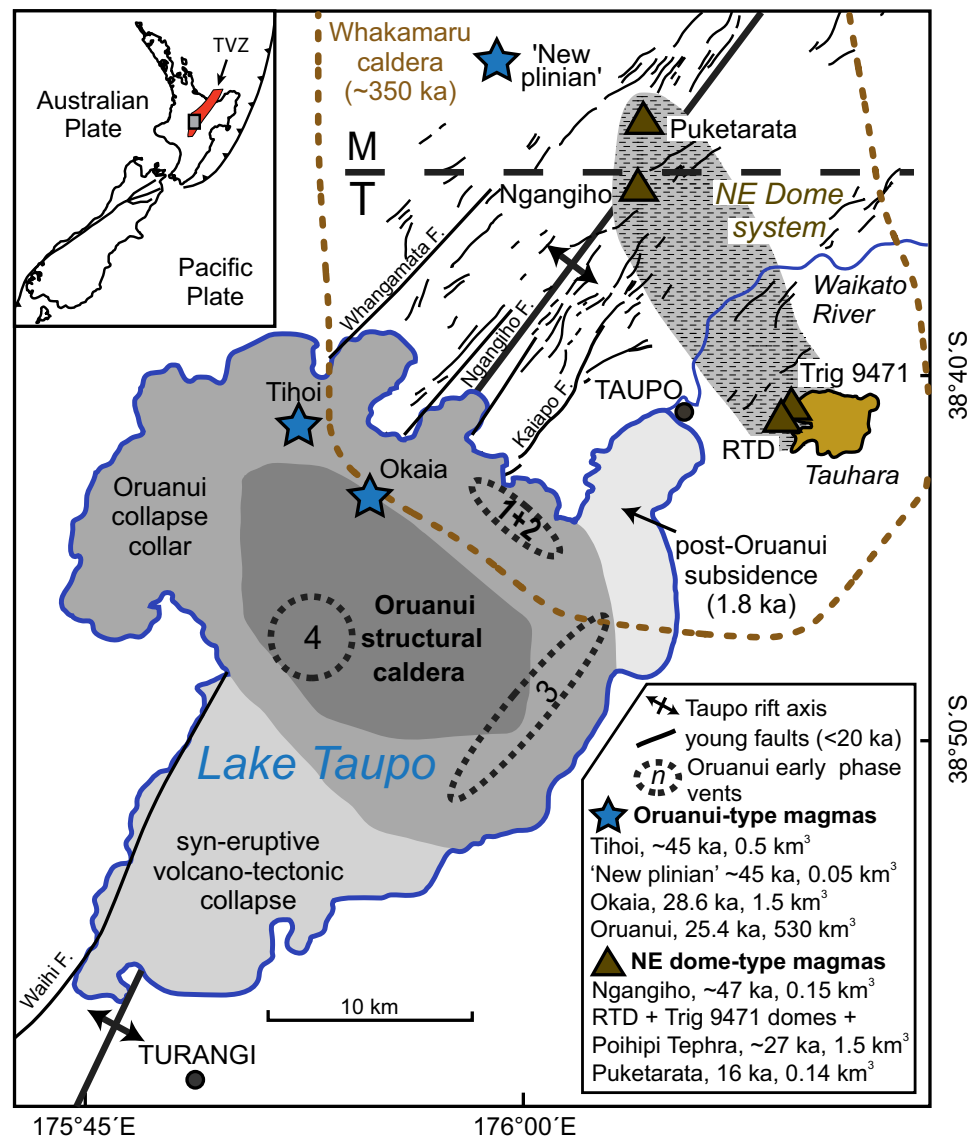
The Oruanui eruption

Eruption summary

The Oruanui eruption at $25,360 \pm 320$ (2 SD) cal year BP (Vandergoes et al. 2013) from Taupo volcano in the central North Island of New Zealand (Fig. 1) is the youngest supereruption on Earth, discharging $\sim 530 \text{ km}^3$ of

moderate- to high-silica rhyolite magma with 3–13 wt% crystals (Wilson 2001; Wilson et al. 2006). Ten eruptive phases are identified, based on bedding and grading characteristics in the fall deposits. The eruption was episodic, with several time breaks varying in duration from probably only hours (i.e. long enough for the eruption plume to have dispersed and ash to wholly settle out before the next phase began), to a period of months between phases 1 and 2 during which time reworking and bioturbation of the earlier ash occurred (Wilson 2001). Extensive interaction of magma with lake water during the eruption caused rapid chilling, extensive fragmentation and produced extremely widely dispersed, fine-grained fall deposits and a large, non-welded ignimbrite (Self and Sparks 1978; Self 1983; Wilson 2001; Van Eaton et al. 2012; Van Eaton and Wilson 2013). The eruption products are fresh, glassy and entirely non-welded, although pumices large enough for detailed

Fig. 1 Key volcanic and tectonic features of the Taupo area, located in the central North Island of New Zealand (see inset: TVZ Taupo Volcanic Zone). Caldera structure and vent areas for phases 1–4 of the Oruanui eruption are from Wilson (2001). The NE–SW alignment of ‘young’ faults (<20 ka: Langridge et al. 2016) form the axis of regional extension in the modern TVZ. Dashed line marks the boundary between Taupo (T) and Maroa (M) volcanoes (Sutton et al. 1995). The stippled grey region encompasses the NE dome magmatic system and associated biotite-rhyolite domes erupted in the last ~ 50 kyr (triangles—after Sutton et al. 1995) Modified from Wilson and Charlier (2009)



study are largely restricted to the ignimbrite. The interbedded nature of the fall deposits and ignimbrite, and spikes in the abundance of juvenile mafic material, allow the eruption phase boundaries to be linked between the fall and flow deposits (Wilson 2001), such that clasts sampled from the ignimbrite can be placed within a time-stratigraphic context.

Juvenile products

Juvenile products of the Oruanui eruption fall into seven categories (five felsic, two mafic; Table 1). By far the most voluminous, comprising ~98% of the total erupted volume, is highly vesicular white pumices of high-SiO₂ rhyolite (HSR hereafter), defined as having whole-rock SiO₂ >74 wt%. HSR clasts characteristically contain 3–13% crystals, have quartz forming 9–21% of the crystal fraction and mostly have more orthopyroxene than amphibole (opx 45–82% to amph 55–18%: Sutton 1995 in Wilson et al. 2006). Sparse (~0.5%), white, low-SiO₂ rhyolite pumices (LSR, whole-rock compositions <74 wt% SiO₂) lack quartz and have more amphibole than orthopyroxene (opx 29–42% to amph 71–58%: Sutton 1995; Wilson et al. 2006). Wilson et al. (2006) originally considered HSR and LSR to represent a compositional continuum, but Allan et al. (2013) inferred that they were separate entities (see also “Results” section below) that only encountered each other syn-eruptively. We focus on these two of the rhyolite types in this paper.

Three additional, volumetrically minor (<<1%) but genetically significant Oruanui rhyolitic components have previously been identified, and are summarised here for completeness. The first is pumices showing a white/pale grey streaky nature, and which fall along a mixing trend between the HSR and more mafic magma (Sutton 1995; Wilson et al. 2006, figure 18). The second is pumices that show enrichment in MgO for a given SiO₂, and have been similarly attributed to mixing of HSR and more mafic magma but the clasts show no signs of mingling in hand specimen (Sutton 1995; Wilson et al. 2006, figure 18). The third is a denser, more crystal-rich, biotite-bearing rhyolite pumice, identified as a ‘foreign’ magma sourced from the nearby but wholly chemically and isotopically independent ‘NE dome’ system (Sutton et al. 1995; Fig. 1). This biotite-bearing magma is interpreted to have been fed laterally by diking from its parental magma system into the Oruanui conduit at the onset of eruption and throughout phases 1 and 2 (Allan et al. 2012), but it has not been identified in later eruption products.

Clasts of juvenile mafic magma from two physically and chemically distinct lineages also occur within the Oruanui deposits: an olivine-bearing calc-alkaline group and a tholeiitic group in which olivine is very rare. Based on

detailed componentry of ash-grade material from the eruption deposits (Wilson 2001), the two mafic lineages together are estimated to represent 3–5 km³ of magma. The relative proportions of the calc-alkaline to tholeiitic end-members are not constrained, although subequal numbers of clasts from each type have been collected. The mafic clasts are inferred to be juvenile on the basis of cauliform or crenulated margins, indicating that they were hot and plastically deforming until quenched on eruption (Wilson 2001; Rooyackers 2015 and manuscript in preparation). The two mafic groups are compositionally distinguished on plots of whole-rock SiO₂ versus FeO_T/MgO with both calc-alkaline and tholeiitic groups being almost entirely contained within the appropriate fields as defined by Miyashiro (1974).

Samples studied

For this study, we collected HSR pumices from early-erupted fall deposits (phases 1 and 2); and from early- (phases 2 and 3), mid- (phase 7) and late-erupted (phase 10) ignimbrite within the stratigraphic framework of Wilson (2001). Wilson et al. (2006) showed that although there was notable compositional variability within the Oruanui rhyolites, the deposits themselves were not systematically zoned with respect to stratigraphic height (Fig. S.1). The melt-dominant magma body, accordingly, was inferred to have undergone thorough mixing at some stage prior to eruption (Wilson et al. 2006). The LSR pumices were sampled from phase 3 ignimbrite at a single location (at the Hinemaiaia C Dam in Lake Taupo Forest: locality 1086 of Wilson 2001), where LSR material was previously observed to be most abundant.

Analytical techniques

Whole rock analytical methods

To expand the data set in Wilson et al. (2006), single clasts of rhyolitic (Allan et al. 2012, 2013, this study) and mafic compositions (this study) were analysed for their bulk chemistries by X-ray fluorescence (XRF) and solution ICP-MS techniques. Clasts were cleaned to remove any adhering matrix, soaked overnight in de-ionised water, and placed in an oven at 110 °C until dry. The mafic clasts, which commonly contained thin adhering rinds of white rhyolite, were coarsely crushed using an agate mortar and pestle, so that fragments of rhyolite could be picked out prior to powdering to ensure characterisation of the mafic end-member. The clasts were then reduced to powder using an agate mill. Whole-rock major element oxide compositions were determined by XRF by either Spectrachem Analytical (CRL Energy LTD, Wellington, New Zealand)

Table 1 Juvenile products of the Oruanui eruption

Magma type	Features	Approx. magma volume	Abbreviations used in this paper	Key references
High-SiO ₂ rhyolite	Whole-rock SiO ₂ >74 wt%; 3–13% crystals; 64–73% plag, 15–21% qtz 7–8% opx, 1.3–5% amph	525 km ³ (>98% of total)	HSR	Wilson et al. (2006), Liu et al. (2006), Allan et al. (2012, 2013)
Low-SiO ₂ rhyolite	Whole-rock SiO ₂ <74 wt%; 6% crystals; 67% plag, 0% qtz 8% opx, 18% amph. Greatest abundance in deposits of phases 3 and 6	0.5 km ³	LSR	Wilson et al. (2006), Allan et al. (2012, 2013)
Biotite-bearing	Biotite-bearing, 12–24% crystals, Rhyolite derived from an adjacent, independent magmatic system during phases 1 and 2	0.03 km ³	BIB	Sutton et al. (1995), Allan et al. (2012)
High-MgO rhyolite	Visually homogeneous pumices that fall along a trend of least evolved tholeiite mafic magma and HSR. Exceedingly rare as hand specimens	negl.	n/a	Wilson et al. (2006)
Streaky/mixed pumices	Streaky mixtures that fall along a trend of least evolved tholeiite mafic magma and HSR. Exceedingly rare as hand specimens	negl.	n/a	Wilson et al. (2006)
Juvenile mafic 1	Calc-alkaline trend, olivine common	1–3 km ³	CA	Wilson et al. (2006), Rooyakkers (2015), Rooyakkers et al. (in prep.)
Juvenile mafic 2	Tholeiitic trend, olivine rare	1–3 km ³	TH	Wilson et al. (2006), Rooyakkers (2015), Rooyakkers et al. (in prep.)

plag plagioclase, *qtz* quartz, *opx* orthopyroxene, *amph* amphibole

or the late John Watson at the Open University, UK. International rock standards BHVO-2 (USGS, Hawaiian basalt), BCR-2 (USGS, Columbia River basalt), and JR1 (GSJ, rhyolite) were analysed during the same sessions at Spectrachem, and WSE (Whin Sill dolerite) and OU-3 (Nanhonon microgranite) at the Open University. Data for the first three standards are summarised in the supplementary material of Allan et al. (2013), and for the two Open University standards in the supplementary material (Table S.2) for this paper. Overall, relative differences from accepted values are BHVO-2: <2% except for MnO (−11%) and P₂O₅ (11%); BCR-2: <2% except for MnO (−10%), Na₂O (−2.5%) and P₂O₅ (5.7%); JR-1: <2% except for TiO₂ (−3.7%), MnO (−11.5%), MgO (23%) and K₂O (5.4%); WSE: <1%; OU-3: <1% except for MnO (1.7%), CaO (4.5%) and Na₂O (1.6%). Overall relative 2 SD precisions are better than 1% for SiO₂, Al₂O₃ and Fe₂O₃, 1–2% for MnO, MgO, CaO, Na₂O and P₂O₅, and 3–5% for K₂O and TiO₂.

Whole-rock trace element compositions were determined using an Agilent 7500CS ICP-MS and Thermo Scientific Element2 sector-field ICP-MS at Victoria University of Wellington. Sample and standard powders were digested using conventional HF + HNO₃ methods. Calculation of trace element concentrations were determined from raw count rates, after correction for off-peak zeros, by reference to the known elemental concentrations of the BHVO-2 whole-rock standard, and utilising ⁴³Ca as the internal standard with the CaO content of samples previously determined to ~1% by XRF. Standards BCR-2, BHVO-2 and JR-1 were analysed under identical conditions and during the same analytical sessions as the Oruanui rhyolitic (Allan et al. 2012) and mafic samples (this study). Data for these standards are available in the online supplementary information of Allan et al. (2012). Overall, relative differences from accepted values are BHVO-2: <1% except for Zn (−5.7%), Tm (1.1%) and Lu (1.4%); BCR-2: <5%, except for Cr (−16%) and Mo (25%); JR-1: <5% except for Yb (5.2%), Er (6.6%), Zr (−7.7%), Ti (−8.6%), Gd (8.6%), Ho (9.2%), Sc (14%), V (−29%), Cr (−40%), Mo (−75%), Zn (78%) and Cu (150%). Average % 2 SD precisions based on analysis of whole rock standards are <3% (MgO, TiO₂, V, Ga, Rb, Sr, Y, Zr, Nb, La); 3–5% (MnO, Ba, Ce, Pr, Nd, Sm, Eu, Gd, Tb, Dy, Ho, Er, Tm, Yb, Lu, Hf, Th, U); 5–10% (Cu, Pb); 10–15% (Sc, Mo, Cs); 15–20% (Zn).

In situ analytical methods

Crystals were liberated from the host felsic clasts by gently crushing in an agate mortar and pestle, then handpicked from the appropriate size fraction and mounted in epoxy resin blocks. Analysis of crystals from the mafic clasts was approached in two ways. (1) Crystals were handpicked

from the 0.5 to 1.0 mm size fraction of crushed material and mounted on epoxy resin blocks. (2) Clasts were thin sectioned so that mineral phases at sizes <0.5 mm could be imaged and analysed within their host groundmasses. All in situ analyses of glass and mineral phases considered here (Allan et al. 2012, 2013, and new data) were undertaken using a JEOL JXA-8230 electron probe microanalyser (EPMA), and a New Wave 193 nm laser ablation system coupled to an Agilent 7500CS ICP-MS at Victoria University of Wellington. Glass analyses by EPMA were conducted at an accelerating voltage of 15 kV and current of 8 nA with the beam de-focused to 10 μm and count times for Na reduced to minimise the effects of alkali-loss. Mineral analyses by EPMA were conducted at 12 nA under a focused electron beam (~2 μm). Prior to in situ analysis of the HSR and LSR mineral phases, high resolution back-scattered electron (BSE) images of each crystal were obtained. These images were used to note crystal textures and zonation features and infer, where possible, a crystal stratigraphy to ensure that at least the inferred oldest and youngest, and most and least evolved, domains of each crystal were targeted for analysis. Standardisation was determined using a series of natural and synthetic standards, chosen to match as closely as possible the matrix composition of the material being analysed. Secondary mineral standards (Engels amphibole, Johnstown hypersthene, NMNH 115900 plagioclase, Kakanui augite, Springwater olivine) and glass standards (ATHO-G, VG-A99, VG-568) were analysed throughout the analytical sessions to monitor signal stability and inform estimates of precision and accuracy.

Trace element analyses by LA-ICP-MS included a minor isotope of a major element (typically ²⁹Si or ⁴³Ca), previously determined by EPMA for use as an internal standard (Pearce et al. 1996). For analysis of the ferromagnesian mineral phases, the USGS basaltic glass standard, BHVO-2G, was used as the calibration standard, whereas NIST612 was used for analysis of plagioclase and melt inclusions. The ICP-MS was tuned by adjusting the positions of the torch, lenses, and the inflow of ultra-pure He while rastering at 2 μm/s across the calibration standard. Data for samples and standards were collected under identical conditions during 60-s acquisitions (plus 60 s for backgrounds), under a static laser beam of 25–35 μm diameter, and pulsed at 5 Hz. Analytical data were reduced using the Iolite software package using the trace element (Internal Standard) data reduction scheme (Hellstrom et al. 2008). The raw time-resolved signal from each analysis was scrutinised to identify and remove any data compromised by the accidental ablation of contaminant (non-targeted) phases, before final trace element contents were calculated. Estimates of precision and accuracy of LA-ICP-MS data were derived from repeat analyses of the glass standards BHVO-2

(USGS Hawaiian basalt), BCR-2G (USGS, Columbia River basalt) and ATHO-G (MPI-DING, Icelandic rhyolite) and are given in supplementary material Table S.3. Overall, relative differences from accepted values are BHVO-2G: <5% except for Sc (−5.7%), Ni (5.6%), Cu (36%), Zn (−9.0%), Tm (−7.1%) and W (−9.0%); BCR-2G: <5%, except for Sc (5.4%), Mn (6.6%), Ni (−7.4%), Cu (−21%), Zn (11%) and W (18%); ATHO-G: <10% except for Mg (17%), Sc (140%), Ti (13%), V (−12%), Cr (−51%), Cu (−15%), Ga (−19%) and Cu (17%). Average % 2 SD precisions based on analysis of glass standards are

- BHVO-2G: <10% (Li, Mg, Sc, Ti, V, Mn, Co, Zn, Ga, Rb, Sr, Y, Zr, Nb, Ba, La, Ce, Pr, Nd, Eu, Tb, Dy, Hf, Ta, Th), 10–20% (Ni, Sm, Gd, Ho, Er, Tm, Yb, Pb, U) and >20% (Cu, Cs, Lu, W);
- BCR-2G: <10% (Li, Mg, Sc, Ti, V, Mn, Co, Zn, Ga, Rb, Sr, Y, Zr, Nb, Ba, La, Ce, Pr, Nd, Eu, Tb, Dy, Ho, Er, Hf, Th, U), 10–20% (Cr, Ni, Sm, Gd, Tm, Yb, Lu, Ta, Pb) and >20% (Cu, Cs, W);
- ATHO-G: <10% (Li, Mg, Mn, Ga, Rb, Sr, Y, Zr, Nb, Ba, La, Ce, Pr, Nd, Tb, Dy, Ho, Er, Yb, Hf, Pb, Th, U), 10–20% (CaO, Sc, Ti, V, Zn, Sm, Eu, Gd, Tm, Lu, Ta, W) and >20% (B, Cr, Co, Ni, Cu, Cs).

Results

Oruanui rhyolite compositions

Whole rock and glass chemistry

Whole-rock rhyolite compositional data are presented by Wilson et al. (2006) and Allan et al. (2013), and a representative suite of the latter data is given in Table 2. A compilation of all existing and new data for the juvenile mafic clasts is in Electronic Appendix 1 and a representative suite of new data is given in Table 3. HSR pumices have relatively uniform glass compositions, but all LSR clasts have bimodal glass compositions (Electronic Appendix 2; Fig. 2a). The more evolved of these is compositionally identical to the HSR matrix glass, and glass from the widespread Oruanui fall deposits (Lowe et al. 2008; Allan et al. 2008; Vandergoes et al. 2013; Table S.4). The presence of the two, non-hybridised glass populations has been interpreted to reflect latest stage entrainment of HSR melt into LSR magma, immediately prior to quenching (Allan et al. 2013). Quartz-hosted melt inclusion data presented here (Electronic Appendix 2) confirm observations by Liu et al. (2006) and Bégué et al. (2015) that inclusions in HSR samples are more evolved than the groundmass glass (Fig. 2b). Although there is some overlap, these data indicate that for at least part of their history most Oruanui quartz crystals

grew from (and trapped) melts that were more evolved than the carrier melts in which they were erupted (i.e. quartz is largely xenocrystic relative to the groundmass pumice glass). The LSR glass data from both plagioclase-hosted melt inclusions and groundmass glass form two trends when Rb/Sr is plotted against Ti content: one with a steeper, higher Ti array, and the other a shallower, lower Ti array (Fig. 2d) along trends towards less evolved compositions.

Textural linkages between crystal phases in the HSR

Backscattered electron (BSE) images of amphibole, pyroxene, plagioclase and Fe–Ti oxides, and cathodoluminescence (CL) images of quartz, reveal textural and zonation features in the main crystal phases, particularly in those of the volumetrically dominant HSR. Allan et al. (2013) noted that ~90% of HSR orthopyroxene showed distinctive core–rim relationships, in which a more Mg- and inclusion-rich core was surrounded by 40–400- μm -thick inclusion-poor rim that was normally zoned with a consistent $\text{En}_{46\pm 2}$ composition in its outermost parts (Fig. 3a). Zonation in individual crystals varies due to combined effects of dissolution and recrystallisation, unequal kinetic/growth zonation and overprinting from Fe–Mg interdiffusion (Allan et al. 2013). The remaining ~10% of HSR orthopyroxenes tended to be inclusion-poor and lacked any significant core–rim zonation.

BSE images of individual HSR plagioclase crystals show that they record a complementary suite of textures to the orthopyroxenes. In total, 89% of the HSR plagioclase crystals ($n = 168$) also have prominent core–rim zonation (Fig. 3b). The cores are typically truncated by at least one episode of resorption and are surrounded by subhedral to euhedral overgrowths that are normally zoned towards an outermost composition of $\text{An}_{38\pm 2}$. Of these zoned crystals, 48% have cores that are patchy/sieve textured, and 41% show significant resorption but no evidence of sieve texturing (Fig. 3b); and they can be further subdivided into those with high An ($>\text{An}_{70}$) cores, and those with prominent blue-grey cores (e.g. Charlier et al. 2008). The remaining 11% of HSR plagioclase are either nominally unzoned (An contents varying by <3 mol %, and accounting for ~7% of all HSR plagioclase), or showed normal, oscillatory zonation with no distinction between core and rim-zones.

The HSR quartz textures in CL images indicate a history that is not directly comparable to those of the plagioclase and orthopyroxene (Fig. 4). Brightness of quartz under CL scales with Ti concentration (Peppard et al. 2001; Wark et al. 2007; Matthews et al. 2012). The causes of varying or oscillating concentrations of Ti in magmatic quartz are debated around fluctuations in temperature (e.g. Wark and Watson 2006; Wark et al. 2007), pressure (Thomas et al. 2010, 2015; Huang and Audétat 2012), and/or the

Table 2 Representative major (XRF) and trace element (ICP-MS) analyses of Oruanui rhyolitic clasts

Sample no.	P1957-3	P1959	P2110F	P1676	P2075	P2059	P1670	P2110C	P2110A	P2110B
Eruption phase	1	1	3	3	7	10	3	3	3	3
SiO ₂	75.90	75.33	76.31	76.76	76.14	75.83	70.80	72.05	72.71	72.39
TiO ₂	0.19	0.22	0.18	0.16	0.20	0.17	0.47	0.40	0.37	0.38
Al ₂ O ₃	13.19	13.30	12.97	12.81	12.84	13.78	14.96	14.56	14.39	14.52
Fe ₂ O ₃	1.72	1.92	1.69	1.60	1.81	1.68	3.25	2.93	2.82	2.87
MnO	0.06	0.06	0.06	0.05	0.06	0.05	0.10	0.10	0.09	0.09
MgO	0.27	0.37	0.26	0.22	0.26	0.20	0.76	0.63	0.59	0.55
CaO	1.65	1.81	1.55	1.42	1.50	1.41	2.81	2.38	2.25	2.33
Na ₂ O	4.04	4.07	3.70	3.68	4.11	3.87	4.35	4.21	3.91	4.05
K ₂ O	2.98	2.90	3.23	3.27	3.04	2.99	2.35	2.63	2.77	2.73
P ₂ O ₅	0.02	0.03	0.04	0.03	0.04	0.02	0.13	0.10	0.09	0.10
LOI	2.82	3.41	3.44	3.36	2.76	3.39	3.91	4.14	4.63	4.47
SUM	96.80	96.15	95.80	96.62	96.63	95.96	95.68	95.14	94.58	94.63
FeO*/MgO	5.82	4.64	5.81	6.54	6.23	7.51	3.84	4.16	4.27	4.73
Li	31	28	13.7	13.5	36	29	16.6	15.5	26	26
Sc	5.7	6.8	5.9	5.3	6.7	6.0	11.9	10.2	10.6	10.1
Ti	1080	1350	1100	970	1270	1030	2820	2420	2300	2230
V	6.0	10.8	5.9	4.7	6.2	4.5	16.0	8.5	9.5	9.6
Cr	1.2	4.3	1.3	0.82	0.54	2.2	1.2	2.4	4.5	3.4
Co	1.3	2.0	1.8	1.2	1.2	1.0	–	–	–	–
Ni	–	–	–	–	1.5	1.3	–	–	–	–
Cu	4.5	4.6	3.1	3.1	3.1	4.1	2.9	4.2	5.8	4.6
Zn	56	62	63	58	46	45	76	79	66	65
Ga	15.2	15.6	15.3	14.8	14.8	15.2	17.8	17.5	17.3	17.1
Rb	102	102	108	110	105	103	72	76	83	79
Sr	129	133	122	113	114	108	213	193	178	186
Y	23	24	24	23	24	22	28	28	28	27
Zr	114	123	112	108	120	114	280	270	264	272
Nb	6.5	6.7	6.6	6.4	7.3	7.0	–	–	–	–
Cs	5.5	5.4	6.1	6.0	4.7	4.4	3.8	4.0	4.4	3.4
Ba	628	604	646	614	658	672	510	539	565	545
La	22	22	23	22	23	21	21	22	21	21
Ce	44	44	47	45	47	45	44	46	45	45
Pr	4.9	5.0	5.2	5.1	5.1	4.8	5.3	5.5	5.3	5.3
Nd	17.8	18.5	19.1	18.5	18.8	17.4	21	22	21	21
Sm	3.6	3.8	3.9	3.8	3.9	3.5	4.6	4.7	4.6	4.5
Eu	0.82	0.84	0.80	0.78	0.82	0.77	1.3	1.3	1.2	1.3
Gd	3.7	3.9	3.9	3.8	3.9	3.6	4.9	4.9	4.7	4.6
Tb	0.57	0.60	0.60	0.57	0.60	0.55	0.76	0.76	0.74	0.72
Dy	3.7	3.8	3.9	3.7	3.9	3.5	4.8	4.8	4.7	4.6
Ho	0.78	0.80	0.80	0.78	0.81	0.74	1.0	1.0	1.0	0.95
Er	2.4	2.5	2.4	2.4	2.5	2.2	3.0	3.0	3.0	2.9
Tm	0.36	0.38	0.37	0.36	0.38	0.34	0.45	0.45	0.45	0.44
Yb	2.5	2.6	2.6	2.6	2.6	2.4	3.0	3.0	3.1	3.0
Lu	0.39	0.40	0.40	0.39	0.39	0.36	0.47	0.47	0.47	0.46
Hf	3.5	3.6	3.4	3.4	3.6	3.6	6.4	6.5	6.4	6.3
Pb	12.7	12.6	13.2	13.1	13.1	13.7	9.9	10.8	11.4	11.0
Th	10.7	10.7	11.1	11.0	10.6	11.3	7.4	8.0	8.6	8.0
U	2.4	2.4	2.5	2.6	2.4	2.4	1.8	1.9	2.0	1.9
Rb/Sr	0.79	0.76	0.88	0.97	0.92	0.95	0.34	0.39	0.47	0.42
Eu/Eu*	0.68	0.67	0.62	0.62	0.65	0.66	0.85	0.84	0.80	0.84

combined influences of temperature, pressure and melt compositions (Wilson et al. 2012). Regardless of the ultimate controls on CL (\approx Ti) zonation in quartz, the Oruanui HSR quartz crystals do not follow an overarching zonation pattern. Some quartz crystals have darker cores and brighter rims, and others show the opposite. Many crystals are multiply zoned with many bright and dark bands, yet some are devoid of any CL zonation at all. In direct contrast to the plagioclase and orthopyroxene, the outermost quartz rims do not appear to converge on a consistent zonation pattern or composition. This is consistent, however, with the analytical data in Liu et al. (2006) and Wilson et al. (2012), where quartz rim analyses show roughly the same mean (\sim 85 ppm) and as wide a range of Ti concentrations (\sim 50 to 120 ppm) as the dataset as a whole, implying that mixing in of quartz crystals from a variety of sources occurred.

Compositional characteristics of crystals in the HSR and LSR

A new suite of mineral analyses has been undertaken for this work to supplement the data in Wilson et al. (2006) and provide the basis for our revised interpretations. Full data sets are presented in Electronic Appendices.

Plagioclase HSR plagioclase crystals (Electronic Appendix 3) have a wide range of anorthite contents from An_{26} to An_{88} , mostly reflecting diverse crystal core compositions (Fig. 5a). The majority of crystal rims, however, converge on a narrow range of $An_{38\pm 2}$. The majority of crystal cores and interiors have compositions that are less evolved (57% are $An_{>42}$), and a minority that are more evolved (12% are An_{26-35}) than the rims. Texturally homogeneous grains (unzoned in BSE imagery) cluster in their composition around those of the rim compositions of the other grains. The LSR plagioclase crystals (Fig. 5b) exhibit a more restricted range of compositions, the majority (94%) ranging between An_{38} and An_{60} . The outermost rims of LSR plagioclase are relatively restricted in composition with 91% of analyses in the range $An_{44\pm 6}$. The LSR plagioclases show steep positive or negative trends between An content and Sr (Fig. 5c) and Ba (Fig. 5d). The same parameters for the HSR crystals show two limiting trends in the cores and interiors data that converge around the compositions of the outermost rims.

Orthopyroxene Major and trace element compositional data for both HSR and LSR orthopyroxenes (after Allan et al. 2013; Electronic Appendix 4) show similar ranges (Fig. 5e–h), with the biggest difference being that the outermost HSR rims grains show a very restricted compositional range (95% are $En_{46\pm 2}$), whereas the outermost LSR rims are generally more variable. HSR orthopyroxene rims have very uniform Al contents, whereas HSR cores and interiors have a significant tail off to higher Al values. The LSR orthopyroxenes show a similar compositional range

to the HSR crystals, but in general a greater proportion of them are in the higher Al range. Ti and Al trend positively with En content, whereas Mn and Zn are anti-correlated with Al (Fig. 5e–h). Overall, there are no major compositional differences between the fields of HSR and LSR orthopyroxenes.

Amphibole The majority of HSR outermost rim compositions (Electronic Appendices 5 and 6) are tightly clustered (47 ± 1 wt% SiO_2 , 1.4 ± 0.2 wt% TiO_2 , 7 ± 1 wt% Al_2O_3 , 12 ± 1 wt% MgO) (Fig. 6). The data from HSR cores plus interiors and LSR amphiboles not only overlap this range but also extend to higher concentrations of TiO_2 and MgO (Allan et al. 2013). The amphibole Eu/Eu* ratio was used by Allan et al. (2013) as a first-order proxy for melt composition, with higher Eu/Eu* values indicating growth from lesser evolved melts and vice versa. Allan et al. (2013, their Fig. 3) reported that concentrations of Mn and Zn show an initial increase with decreasing Eu/Eu* but then their abundance decreases below Eu/Eu* of \sim 0.45. Similar noteworthy inflections in the abundances of Eu (going from static to decreasing abundances: Fig. 6b), Ni and Co (going from static to increasing abundances: Fig. 6c, d) are also evident around this same hinge point. Eu/Eu* ratios of the amphiboles are linearly and positively correlated (R^2 of 0.83: Allan et al. 2013) with the apparent pressures of amphibole crystallisation derived from the calibration of Ridolfi et al. (2010). The abundances of elements such as Mn, Eu, Ni and Co when plotted against model pressures suggest that changes in amphibole chemistry occurred once the amphiboles crystallised at model pressures of <140 – 160 MPa, equivalent to depths of \sim 6 km.

Intensive variables

Estimates of Oruanui magma intensive variables and water contents have been made through a variety of measurements and models. The results of preferred thermometric models, i.e. those that gave realistic, consistent and reproducible temperature estimates, are summarised in Table 4 and Fig. S.2. Analytical data for Fe–Ti oxides are given in Electronic Appendix 7. Application of the Ghiorso and Evans (2008) model (using the EPMA correction factors from Evans et al. 2006) to equilibrium pairs (after Bacon and Hirschmann 1988) yielded mean temperatures of 790 and 840 °C for the HSR and LSR magmas, respectively. The same Fe–Ti oxide pairings applied to the Sauerzapf et al. (2008) model yield temperatures \sim 15–25 °C higher. Despite the offset between the two Fe–Ti oxide models, both indicate a \sim 40–50 °C difference between the final pre-eruptive temperatures of the HSR and LSR magmas.

Table 3 Representative major (XRF) and trace element (ICP-MS) analyses of Oruanui juvenile mafic clasts

Sample no. Group	P554 TH	P1975 TH	P581 TH	P1974 TH	P574 TH	P1976 TH	P1643 CA	P919 CA	P1664 CA	P987 CA
SiO ₂	52.27	54.83	56.52	58.05	62.43	64.47	56.66	56.74	57.90	60.53
TiO ₂	1.44	1.31	1.68	1.24	1.02	0.79	0.79	0.80	0.67	0.78
Al ₂ O ₃	16.92	16.54	17.67	16.71	16.59	14.89	17.84	17.25	17.74	16.61
Fe ₂ O ₃	12.60	11.04	9.60	8.81	6.30	6.86	7.56	7.83	6.91	6.53
MnO	0.19	0.17	0.18	0.16	0.15	0.12	0.14	0.15	0.12	0.14
MgO	4.57	3.89	3.20	3.07	2.03	2.27	4.47	4.45	4.92	3.70
CaO	8.13	7.62	5.98	6.53	5.23	4.94	8.31	8.69	7.44	6.59
Na ₂ O	3.28	3.51	4.30	4.06	4.46	3.70	3.15	3.06	3.16	3.67
K ₂ O	0.48	0.77	0.74	0.96	1.40	1.78	0.85	0.83	0.97	1.22
P ₂ O ₅	0.11	0.33	0.14	0.41	0.40	0.19	0.23	0.20	0.17	0.22
LOI	1.80	0.80	2.22	1.01	1.22	1.47	0.91	0.76	1.23	1.46
SUM	100.30	99.31	100.32	99.07	99.36	98.55	99.06	98.57	98.78	99.18
FeO*/MgO	2.48	2.55	2.70	2.58	2.79	2.72	1.52	1.58	1.26	1.58
Li	10.7	14.7	13.4	16.0	11.7	23.1	14.5	13.5	12.8	15.0
Sc	40	32	28	28	21	21	28	30	25	23
Ti	8550	7820	9610	7740	6440	4890	4710	4710	4200	4350
V	364	272	123	163	78	159	154	162	122	102
Cr	4.7	3.8	0.76	3.1	1.8	8.6	102	111	100	85
Co	28	22	9.6	13.7	7.5	14.1	21	21	22	15
Ni	3.6	2.3	2.0	1.7	1.9	2.0	21	18.4	41	20
Cu	12.9	14.3	6.0	6.8	4.8	13.5	14.6	14.5	13.8	8.6
Zn	106	94	107	93	83	69	74	75	81	74
Ga	21	20	22	20	20	17.9	18.2	17.9	17.6	18.0
Rb	10.6	19.7	20	27	44	60	26	24	35	38
Sr	338	332	367	333	312	237	295	271	267	271
Y	17.3	20	20	24	27	22	20	20	19.3	22
Zr	90	114	204	180	231	110	149	138	154	187
Nb	2.7	3.5	6.2	5.1	6.8	5.5	4.0	3.8	4.2	5.1
Cs	0.41	0.98	0.83	1.3	1.8	3.1	0.96	0.96	1.7	1.5
Ba	152	200	279	253	365	405	313	212	285	302
La	5.1	9.3	8.3	11.9	16.3	15.7	10.0	9.6	9.7	12.7
Ce	14.5	21	19.6	27	36	33	23	22	22	28
Pr	1.8	2.9	2.5	3.6	4.5	3.9	3.0	2.8	2.8	3.5
Nd	8.6	12.8	11.0	16.0	19.3	15.9	12.9	12.4	11.9	15.1
Sm	2.5	3.2	3.0	4.0	4.6	3.5	3.2	3.1	2.8	3.7
Eu	1.1	1.3	1.4	1.5	1.5	1.1	1.2	1.1	1.1	1.3
Gd	2.8	3.5	3.4	4.4	5.0	3.7	3.6	3.5	3.2	3.9
Tb	0.48	0.55	0.56	0.68	0.74	0.58	0.56	0.54	0.51	0.61
Dy	3.1	3.5	3.7	4.3	4.7	3.7	3.6	3.5	3.3	3.9
Ho	0.67	0.73	0.76	0.87	0.97	0.77	0.75	0.73	0.69	0.81
Er	1.9	2.1	2.2	2.5	2.8	2.3	2.2	2.1	2.0	2.4
Tm	0.27	0.31	0.32	0.36	0.40	0.34	0.32	0.31	0.30	0.34
Yb	1.8	2.0	2.2	2.4	2.7	2.3	2.1	2.1	2.0	2.3
Lu	0.27	0.29	0.32	0.36	0.41	0.35	0.32	0.32	0.31	0.35
Hf	2.3	2.7	4.6	4.0	5.2	3.0	3.4	3.2	3.5	4.2
Pb	3.4	6.4	8.2	4.9	7.0	14.4	4.0	4.1	5.2	5.9
Th	1.5	2.1	3.1	3.0	4.8	6.2	2.8	2.7	3.4	4.0
U	0.38	0.53	0.73	0.73	1.2	1.4	0.67	0.65	0.84	0.97
Rb/Sr	0.03	0.06	0.05	0.08	0.14	0.25	0.09	0.09	0.13	0.14
Eu/Eu*	1.30	1.13	1.31	1.10	1.01	0.90	1.06	1.00	1.07	1.01

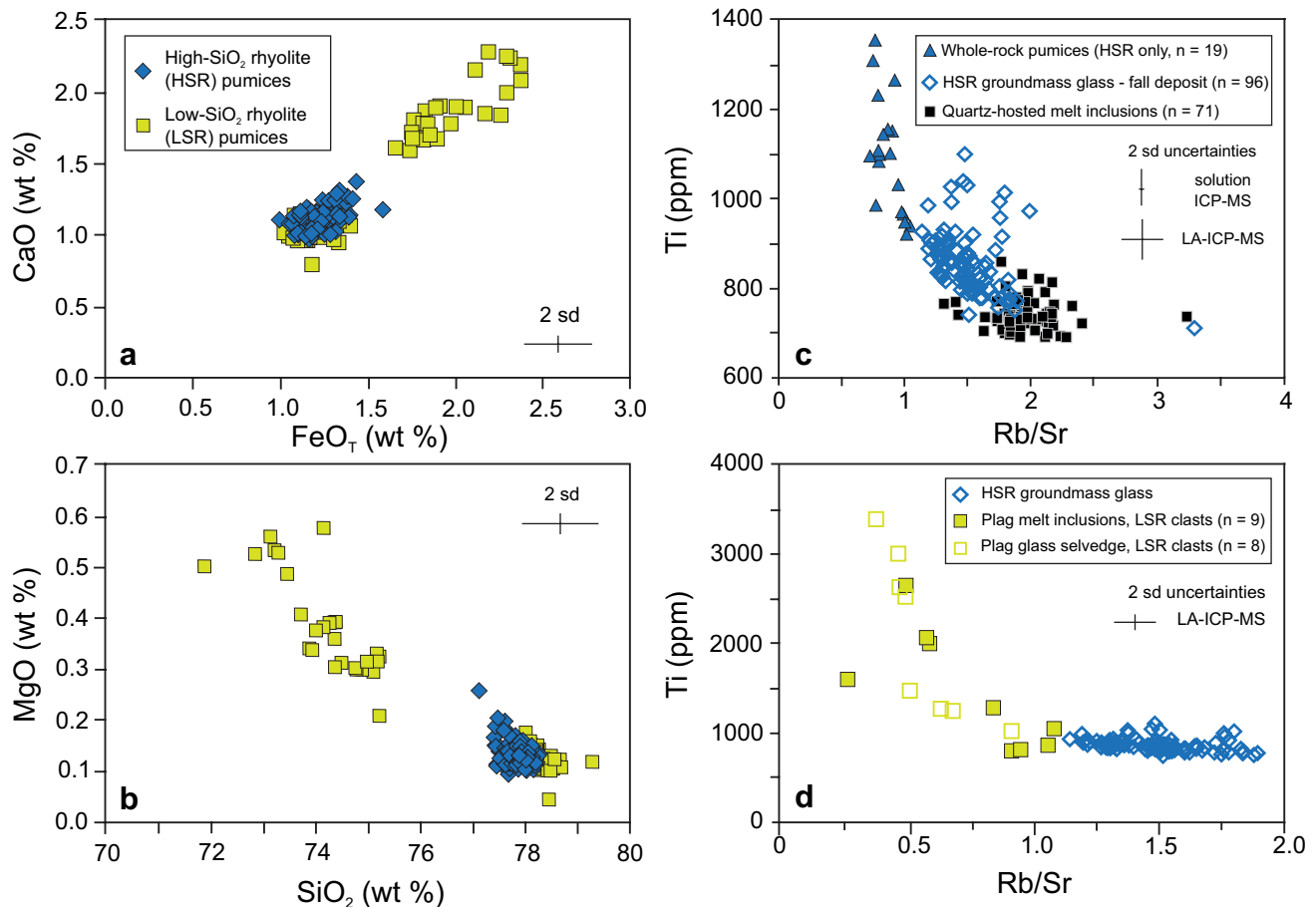


Fig. 2 **a** CaO versus Fe_2O_3 and **b** MgO versus SiO_2 data from fragments of pumice matrix glass in Oruanui high-silica rhyolite (HSR) and low-silica rhyolite (LSR) clasts (see text for definitions). All LSR clasts contain bimodal glass compositions, the most evolved of which corresponds to that of the HSR clasts. The lack of a mixing/mingling relationship between the two groups of compositions suggests that the two rhyolite magmas only encountered each other syn-eruptively. **c** Ti versus Rb/Sr of (whole-rock) HSR pumices, HSR groundmass glass, and quartz-hosted melt inclusions. The majority of quartz-hosted melt inclusions record more evolved compositions (higher Rb/

Sr ratio and lower concentrations of compatible elements) than the groundmass glass. Data sources: HSR pumice (Allan et al. 2012 and this paper); quartz-hosted melt inclusions (this paper); HSR groundmass glass from Allan et al. (2008) and Vandergoes et al. (2013). **d** Ti versus Rb/Sr of Oruanui rhyolite glasses. The HSR groundmass glass data here are from the distal fall deposits where single glass shards are large enough for analysis by LA-ICP-MS (>40 μm thick). The LSR glass values are from selvages on, and melt inclusions in, plagioclase crystals in LSR clasts. Note the two distinct trends in LSR glass compositions

The compositions of outermost amphibole rims for the HSR and LSR magmas, using the Si^* parameter of Ridolfi et al. (2010, equation 1), yielded mean temperatures of 784 and 843 $^\circ\text{C}$, respectively. However, both rhyolite groups are skewed by a subordinate component of crystal rims that tail off to higher temperatures. Prominent model temperature modes centre on ~ 770 – 780 $^\circ\text{C}$ (HSR rims) and ~ 830 $^\circ\text{C}$ (LSR rims; Table 4; Fig. S.2). The plagioclase-melt and orthopyroxene-melt thermometers of Putirka (2008, equations 24a and 28a, respectively), were applied to the compositions of outermost crystal rims (Allan et al. 2013) and matrix glass. Plagioclase-melt and orthopyroxene-melt thermometry yielded mean estimates of 787 and 785 $^\circ\text{C}$, respectively, for HSR samples, and

mean estimates of 831 and 830 $^\circ\text{C}$, respectively, for LSR samples.

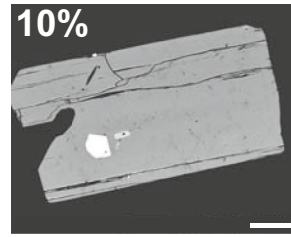
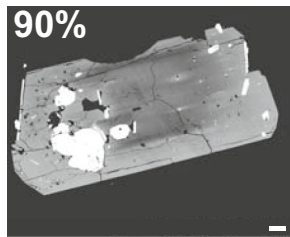
Estimates of the final pressures for storage and crystallisation of the Oruanui rhyolites were determined using the total-Al-based formulation of Ridolfi et al. (2010; their equation 4) applied to outermost amphibole rim compositions (Fig. S.3). Based on these compositions only, HSR samples yielded a mean model pressure of 113 MPa (range 88–185 MPa), with a prominent mode between 90 and 120 MPa. The mean model pressure for LSR amphibole rims was 174 MPa (range 114–243 MPa). As with the HSR amphiboles, the mode of the estimates is slightly lower than the mean. These amphibole-derived pressures for the HSR are consistent with those estimated from concentrations

a

Orthopyroxene in HSR clasts

Prominent zonation

Comparatively Mg-rich core, rich in melt and mineral inclusions, and variably modified by dissolution, recrystallisation and diffusion
40-400 µm thick rim-zones grade out to En_{46±2} in the outermost rims.

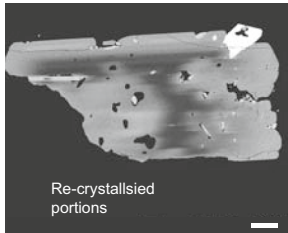


No core-rim zonation

Inclusion-poor crystals with no clear core-rim relationship.
No significant zonation in backscattered electron images.

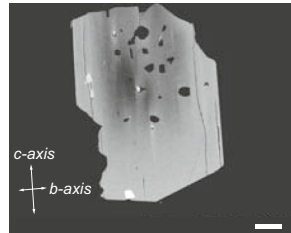
Zoned subgroups

Heavily recrystallised cores



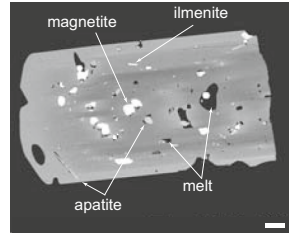
Re-crystallised portions
Feature seen to some extent in all 'cored' Opx. Typically evident around melt and mineral inclusions.

Streaky, discontinuous zonation parallel to c-axis



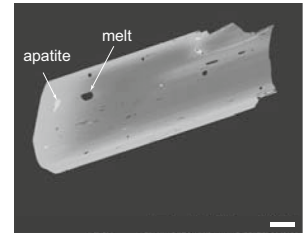
Feature seen in all 'cored' Opx but is most evident in examples with inclusion-rich cores.

Inclusion-rich cores



Common inclusions, in order of decreasing abundance, include magnetite, melt, apatite, and ilmenite, with very rare zircon.

Inclusion-poor cores



Common → Rare
Common inclusions, in order of decreasing abundance, include magnetite, melt, apatite, and ilmenite, with very rare zircon.

b

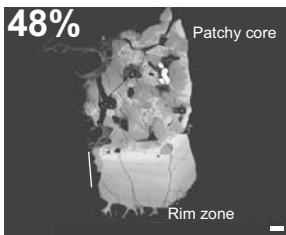
89%

Plagioclase in HSR clasts

11%

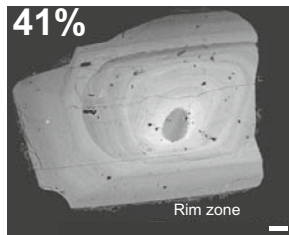
Prominent zonation

Patchy/sieve textured ± resorbed cores



Normally zoned outward toward compositions of An_{38±2}

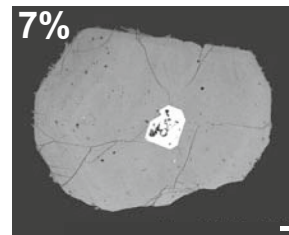
Resorbed cores
NO patchy/sieve texture



Normally zoned outward toward compositions of An_{38±2}

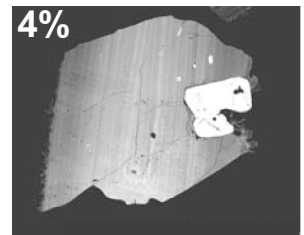
No overarching core-rim zonation

Nominally unzoned



Lack prominent core-rim zonation

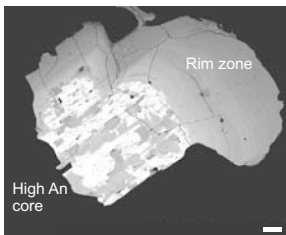
Normal, oscillatory zoned



Sub-groups within 'cored' plagioclase

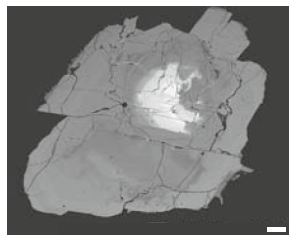
4.5% (of cored plag)
High-An (>An₇₀) cores

Patchy/sieve textured ± resorbed cores



High An cores inherited from mafic magmas

Resorbed cores
NO patchy/sieve texture

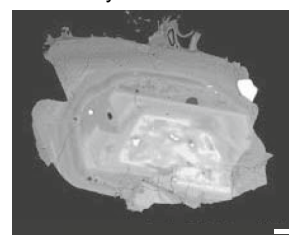


High An cores inherited from mafic magmas

Sub-groups are not mutually exclusive

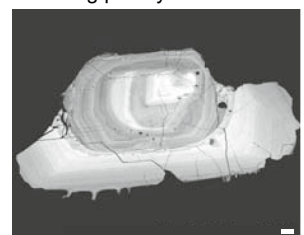
6% (of cored plag)
Blue-grey cored plagioclase

Patchy/sieve textured



Blue-grey cored plagioclase interacting with greywacke melts

Lacking patchy/sieve texture



Blue-grey cored plagioclase interacting with greywacke melts

Fig. 3 a Pictorial summary of the textural and zonation characteristics of orthopyroxene from Oruanui HSR clasts. See text for descriptions. *White scale bars* are 100 μm . **b** Pictorial summary of the textural and zonation characteristics of plagioclase crystals from Oruanui HSR clasts. See text for descriptions *White scale bars* are 100 μm

of H_2O and CO_2 in trapped quartz-hosted melt inclusions (Liu et al. 2006) which have a mean pressure of 138 MPa (range 94–188 MPa). Broadly similar pressure estimates were also presented by Bégué et al. (2014), using rhyolite-MELTS compositions from Oruanui (HSR) quartz-hosted melt inclusions.

Estimates of the final oxygen fugacity for the HSR and LSR magmas were calculated using amphibole rim compositions (Ridolfi et al. 2010; their equation 2), and Fe–Ti oxide equilibrium pairs (Ghiorso and Evans 2008; Sauerzapf et al. 2008) (Table 5). Use of the Ghiorso and Evans (2008) model for Fe–Ti oxides in HSR clasts yields a mean estimate of -0.2 NNO, compared to a mean of $+0.47$ NNO when the Sauerzapf et al. (2008) model is used. The Ridolfi et al. (2010) formulation applied to amphibole rims yields a mean value of $+0.9$ NNO. Mean oxygen fugacity calculated for the LSR samples were as follows: -0.1 NNO (Ghiorso and Evans 2008, model); $+0.4$ NNO (Sauerzapf et al. 2008); $+0.5$ NNO (Ridolfi et al. 2010).

Measurements and estimates of the mean water content of the Oruanui HSR magma vary from 4.5 to 6.2 wt% (Table 5). The lowest values come from FTIR measurements of H_2O in quartz-hosted melt inclusions (Liu et al. 2006). The higher estimates are inferred from amphibole rim compositions (Ridolfi et al. 2010; their equation 3), empirical modelling of H_2O solubility applied to Oruanui HSR compositions (Moore et al. 1998) and plagioclase-melt equilibrium models (Housh and Luhr 1991; Waters and Lange 2015).

Oruanui mafic compositions

Whole rock chemistry

Mafic clasts analysed in here and previously (Wilson et al. 2006; Rooyakkers 2015) range between 50 and 65% SiO_2 , in distinct tholeiitic (higher Fe, Ti) and calc-alkaline (lower Fe, Ti) groups (Fig. 7a; Table 3). New trace element data show that many of the mafic clasts notably have Eu/Eu^* values around or greater than 1 (Fig. 7b).

Compositional characteristics of crystals in mafic clasts

As previously stated, in situ analysis of crystal phases from the mafic clasts was approached in two ways, either

on handpicked separates, or from thin sections of slabbed material. In general the sectioned samples contain greater proportions of smaller sized and more primitive crystals (higher En orthopyroxene, lower SiO_2 amphibole, higher An plagioclase). The distribution of the data sets for sectioned clasts (analysed by EPMA only) versus handpicked separates (EPMA + LA-ICP-MS) in Fig. 8 highlights that the trace element dataset for crystals from the mafic clasts may under-represent the abundance of less evolved crystals as an artefact of the crystal size fraction used for LA-ICP-MS analysis. Plagioclase data appear to be most affected by this apparent sampling bias, with no plagioclase from mafic clasts with FeO_t contents greater than 0.5 wt% having been analysed by LA-ICP-MS (Fig. 8b). It is also apparent that most of the major element compositional ranges in the larger crystals fall entirely within the compositional fields defined by the corresponding crystal species in the HSR and LSR rhyolites. Linkages between plagioclase textures and major element chemistries show several features (Fig. 9). The majority of analyses that returned high Fe contents at a given An content were almost exclusively analyses on groundmass plagioclase (microlites) or from very thin (<5 μm) quench crystallisation rims on larger crystals (see also Rooyakkers 2015 and manuscript in preparation). Of the plagioclase crystals that are consistent with derivation from the rhyolites (i.e. overlapping the compositional fields for HSR and LSR crystals), most show thin rims that increase markedly in BSE brightness (i.e. higher An) reflecting their late-stage immersion in hotter, more mafic melt compositions (e.g. CA_P919 plag 16 in Fig. 9). Others have thicker (>100 μm) rim-zones of mottled high An surrounding relatively featureless more sodic cores (e.g. CA_P987 plag 2 in Fig. 9), possibly indicating a more prolonged exposure to mafic magma.

Olivines from calc-alkaline clasts are almost entirely unzoned with respect to BSE imagery and major element composition, and returned uniform compositions of $\text{Fo}_{85\pm 1}$ (Electronic Appendix 8). However, the outermost rims of these olivines had very thin (<5 μm) BSE-brighter, more Fe-rich rims of Fo_{74} . Olivine is rare in the tholeiitic clasts but three examples gave compositions between Fo_{75} and Fo_{65} . Rare clinopyroxene crystals ranged from En_{34} to En_{49} and Wo_{32} to Wo_{44} (Electronic Appendix 8). The trace element compositions of plagioclase, orthopyroxene and amphibole from the mafic clasts fall almost entirely within the corresponding HSR and LSR crystal fields making identification of crystals considered to be phenocrystic in the mafic magmas difficult (Figs. 10 and S.4). Notable exceptions to this in the calc-alkaline clasts are the very high-An plagioclase (An_{85-95}), and in the tholeiitic clasts the high-En orthopyroxenes and some of the least evolved amphiboles ($\text{Eu}/\text{Eu}^* > \sim 0.8$).

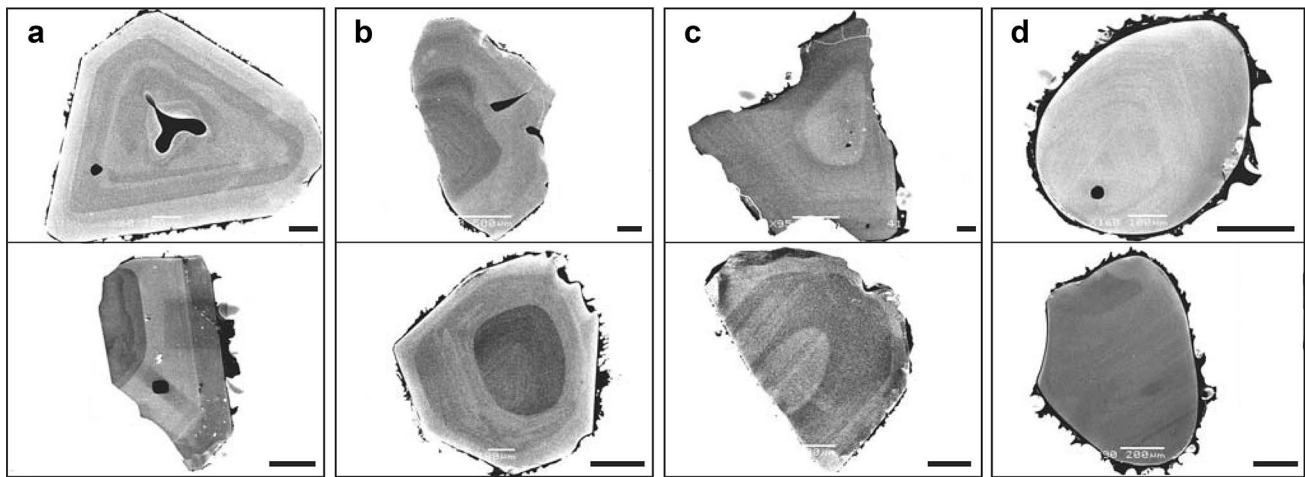


Fig. 4 Representative examples of quartz zonation under cathodoluminescence (CL) imagery. **a** Multiply zoned crystals; **b** dark CL cores, bright CL rims; **c** bright CL cores, dark CL rims; **d** nominally unzoned. The *black scale bars* are 200 μm

Intensive variables

Constraining magma intensive variables in the Oruanui mafic magmas is challenging because the compositional and textural data indicates that many of the crystals in the mafic clasts are not equilibrium phases. Of the models and phases available to constrain pre-eruptive temperatures, Fe–Ti oxides may be considered the most appropriate because they are known to re-equilibrate very rapidly at magmatic temperatures (typically days to weeks; e.g. Freer and Hauptman 1978; Hammond and Taylor 1982; Venezky and Rutherford 1999). Temperatures calculated from equilibrium pairs (after Bacon and Hirschmann 1988) of Fe–Ti oxides from the mafic samples return bimodal temperature estimates centred around 1000 and 840 $^{\circ}\text{C}$ (Fig. 11). This bimodality suggests that there are Fe–Ti oxides from both the mafic and rhyolitic end-members in the mafic clasts. We do not use the Ridolfi et al. (2010) thermobarometric formulations for the mafic amphiboles because the larger crystals are clearly inherited from the rhyolite and the groundmass amphiboles are inferred to have grown under disequilibrium conditions during rapid crystallisation (Rooyackers 2015). Two-pyroxene thermometry has been applied by pairing together clinopyroxene (inferred to be phenocrystic) and the most primitive orthopyroxenes (i.e. those with compositions that are only found in the mafic clasts). When only pairings that pass the Fe–Mg exchange equilibrium test of Putirka (2008) (i.e. $K_D = 1.09 \pm 0.14$) are used, average temperatures of ~ 1010 or 1038 $^{\circ}\text{C}$ are calculated using the Brey and Kohler (1990) and Putirka (2008) models, respectively ($n = 19$; Fig. 11b).

Discussion

The diversity of crystal textures and compositions presented in this study highlights the wide range in magma compositions and intensive conditions within the pre-eruptive Oruanui magmatic system. Wilson et al. (2006) demonstrated that although there was significant whole-rock compositional diversity in the Oruanui rhyolitic clasts, there were no systematic changes in composition with respect to eruption phase (i.e. stratigraphic height; Fig. S.1) and, therefore, no systematic zonation within the immediately pre-eruptive Oruanui melt-dominant magma body. This is confirmed by HSR crystal rims that converge to uniform compositions for each eruptive phase, whether the earliest (phase 1) or latest (phase 10) or vented from different areas within what became the Oruanui caldera (Fig. S.5). Below we consider a sequence of events that led to this final uniformity from what was originally a diverse magma reservoir, and examine factors that governed the development, storage and evacuation of the 530 km^3 Oruanui melt-dominant magma body.

Generation of the Oruanui melt-dominant magma body from a zoned crystal mush

On the basis of amphibole and orthopyroxene textural and chemical data, combined with P–T–H₂O constraints, Allan et al. (2013) proposed that the Oruanui HSR magma body had accumulated following rapid decompression and extraction of large volumes of melt (plus entrained crystals) from a crystal-rich mush-like source body. The significant

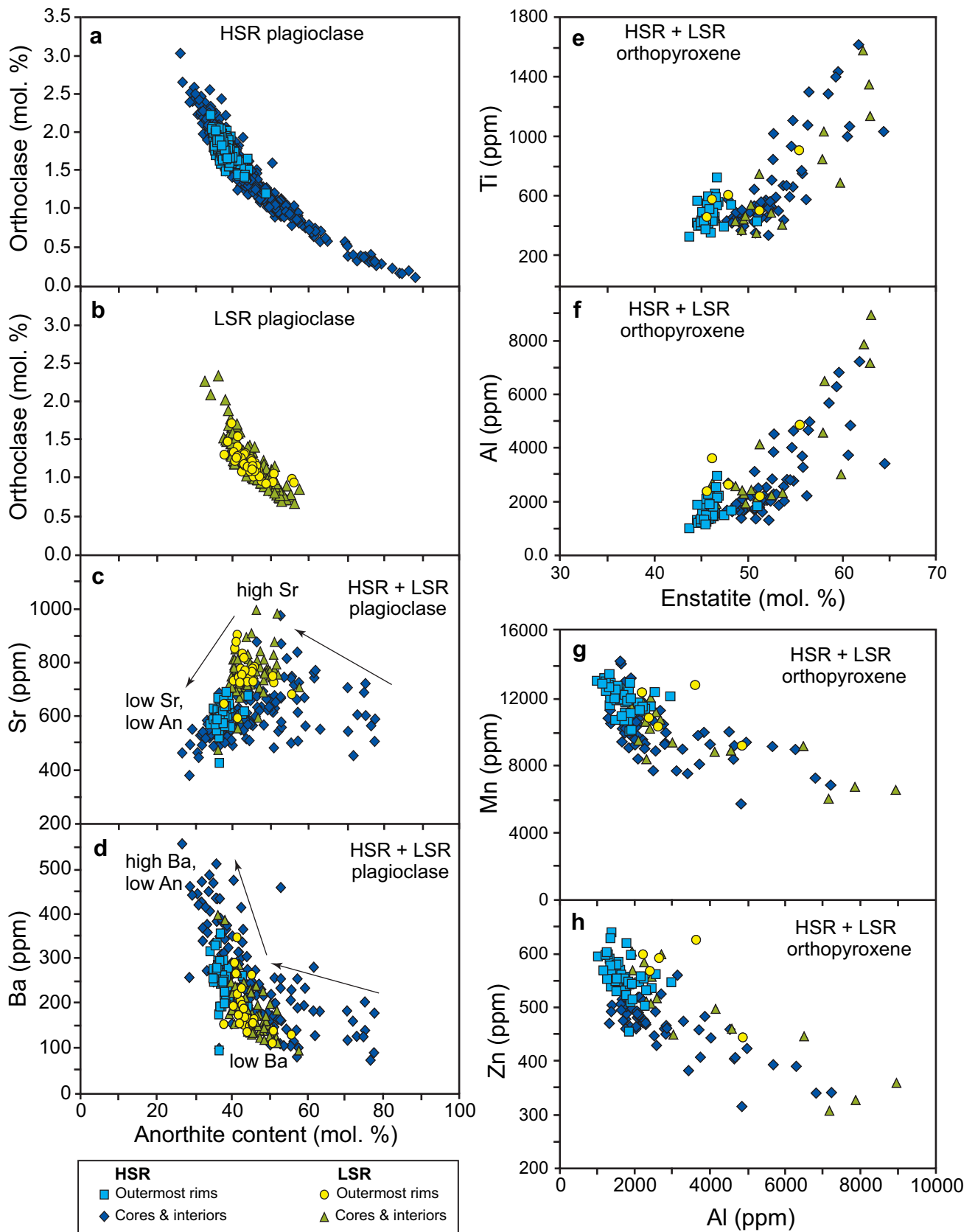


Fig. 5 Selected major element compositional data for plagioclase from **a** HSR and **b** LSR clasts, and **c**, **d** selected trace element data versus An content of plagioclase from HSR and LSR pumices. **e**, **f**

Concentrations of Ti and Al versus mol% En for orthopyroxene from HSR and LSR clasts. **g**, **h** Concentrations of Mn and Zn versus Al content for orthopyroxenes from HSR and LSR clasts

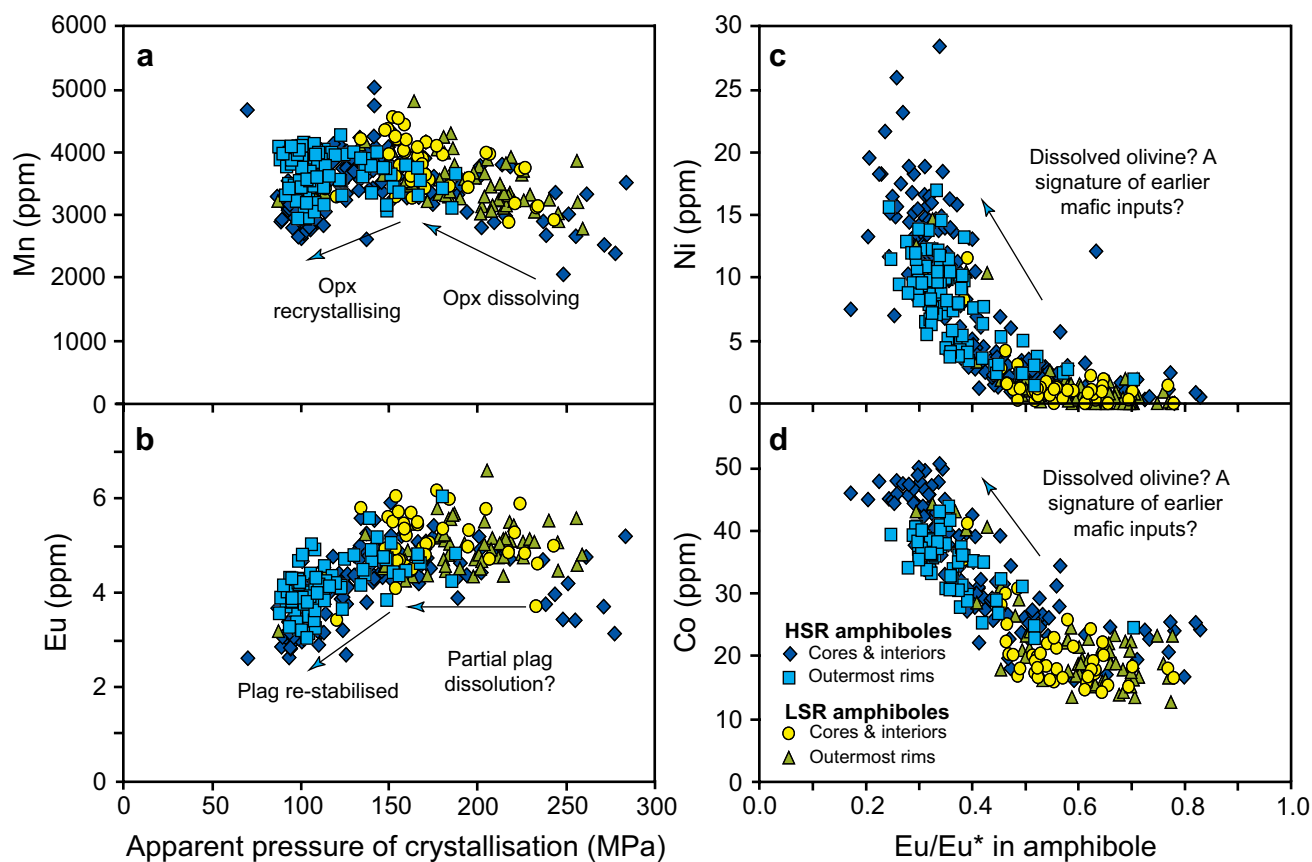


Fig. 6 Selected trace element concentration data for amphiboles from HSR and LSR clasts (symbols are as in Fig. 5). Data shown in **a**, **b** are plotted against the apparent crystallisation pressure as modelled by the Ridolfi et al. (2010) total-Al barometer and in **c**, **d**

against the Eu/Eu^* of the amphibole as a qualitative measure of evolution of the melt from which the amphibole grew. The origins of trends marked in each panel are discussed in the text

Table 4 Summary of estimates for the pre-eruptive temperature of the Oruanui melt-dominant magma body yielded by various mineral equilibrium-based techniques

Estimates of outermost rim crystallisation temperatures (T °C)	Number of estimates	Mean temp (°C)	Temp range (°C)	Modal values	Model details and/or parameters
HSR magma					
Plag-melt (rims)	158	787	783–797		Putirka (2008), equation 24a, matrix glass and 5.5 wt% melt H_2O
Opx-melt (rims)	222	785	779–793		Putirka (2008), equation 28a, matrix glass and 5.5 wt% melt H_2O
Amphibole compositions (rims)	121	784	751–851	770–780	Ridolfi et al. (2010) model
Fe–Ti oxides	378	796	765–836	790	Ghiorso and Evans (2008) model
LSR magma					
Plag-melt (rims)	47	831		820–840	Putirka (2008), equation 24a, matrix glass and 6 wt% melt H_2O
Opx-melt (rims)	49	830		820–840	Putirka (2008), equation 28a, matrix glass and 6 wt% melt H_2O
Amphibole compositions (rims)	59	837	783–903	820–850	Ridolfi et al. (2010) model
Fe–Ti oxides	61	840	812–910	840	Ghiorso and Evans (2008) model

Table 5 Summary of oxygen fugacity and melt H₂O estimates for the final pre-eruptive conditions in the Oruanui HSR and LSR magmas

Estimates of oxygen fugacity (ΔNNO)	<i>n</i>	Mean (ΔNNO)	Range (ΔNNO)	Model details and/or parameters
HSR magma				
Fe–Ti oxides	379	−0.20	−0.52 to 0.03	Ghiorso and Evans (2008)
Amphibole rims	121	0.90	0.40 to 1.20	Ridolfi et al. (2010)
LSR magma				
Fe–Ti oxides	59	0.5	0.2 to 0.8	Ghiorso and Evans (2008)
Amphibole rims	59	0.5	0.2 to 0.8	Ridolfi et al. (2010)
Estimates of H ₂ O melt (wt %)	<i>n</i>	Mean (wt %)	Range	Model details and/or parameters
HSR magma				
Amphibole rims	121	5.5	5.0 to 6.2	Ridolfi et al. (2010) model
Quartz-host melt inclusions	66	4.5	3.8 to 5.1	Liu et al. (2006), H ₂ O in quartz-hosted melt inclusions measured by FTIR
Empirical H ₂ O solubility model	–	5.2	3.9 to 6.6	Moore et al. (1998), model run at 796 °C and 90–240 MPa, mean value at 150 MPa
Glass H ₂ O by difference	141	4.5	0.6 to 7.4	Difference from 100 wt% of raw EPMA totals for pumice matrix glass
Plag-melt equilibrium		4.6		Anorthite-method of Housh and Luhr (1991), reported in Wilson et al. (2006)
Plag-melt equilibrium		6.2		Albite-method of Housh and Luhr (1991), reported in Wilson et al. (2006)
Plag-melt equilibrium		5.5		Method of Waters and Lange (2015) with 790 °C and outer rim values of An _{38±2}
LSR magma				
Amphibole rims	59	6.0	5.6 to 6.5	Ridolfi et al. (2010) model
Plag-melt equilibrium		5.3		Method of Waters and Lange (2015) with 840 °C and outer rim values of An ₄₄

decompression event is reflected in the in situ chemistry of amphibole cores and interior zones which were interpreted to record a chemical signature of the dissolution–recrystallisation history that is texturally evident in orthopyroxene crystals (Fig. 3a). Orthopyroxene destabilisation occurred during decompression from as much as 270 to ~140 MPa, and is recorded in the amphiboles as increasing levels of Mn and Zn, two elements notably enriched in the orthopyroxenes and inferred to have been taken up in the amphiboles as the orthopyroxenes dissolved (Fig. 6a). Decompression to less than ~140 MPa saw the re-stabilisation and regrowth of orthopyroxene rims and a decrease in the abundance of Mn and Zn in the co-crystallising amphiboles.

New data presented here for plagioclase crystals further support the interpretation of rapid extraction and melt accumulation. The significant resorption ± sieve texturing of ~90% of the plagioclase cores, followed by overgrowths of rim-zones (Fig. 3b) are inferred to represent a disequilibrium-then-regrowth history parallel to that experienced by 89% of the orthopyroxenes (Fig. 3). The presence of resorption zones and raddled cores in the feldspars could represent a decompression event or interaction with hotter, less evolved melts within the mush zone, including those parental to the erupted mafic clasts. Experimental studies on andesitic compositions

have shown that sieve-textures similar to that observed in the HSR plagioclase cores can form in response to rapid decompression under fluid-undersaturated conditions (Nelson and Montana 1992). Detailed consideration of the blue-grey-cored plagioclases by Charlier et al. (2008; Fig. 3b) showed that these cores had been partially resorbed, then interacted with hotter melts (including those of metasedimentary crustal origin) to yield dusty textures (cf. Tsuchiyama 1985) in some cases before overgrowth of rims zoned out to the common An_{38±2} range. A general origin for the raddled cores through rapid growth is unlikely because these cores span a wide variety of compositions, indicating that their original growth occurred under a variety of conditions, and the inclusions crosscut the growth zones, indicating that they are a superimposed feature (cf. Nelson and Montana 1992). The notable decrease in the abundance of Eu in the amphiboles at ~140 MPa is commensurate with the inflection of Mn concentrations (Fig. 6a, b) that Allan et al. (2013) interpreted to reflect the re-stabilisation and regrowth of orthopyroxene upon reaching the accumulating melt-dominant magma body. The decrease in Eu content of the amphiboles may similarly reflect the restabilisation and crystallisation of plagioclase in the melt-dominant magma body following the decompression experienced by the host magma parcel.

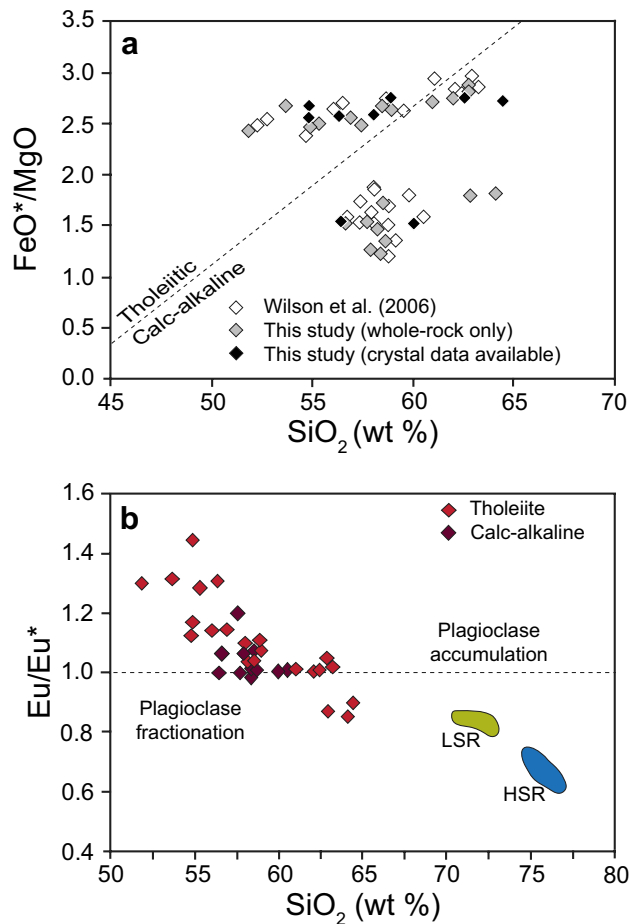


Fig. 7 Selected whole-rock analytical data for single Oruanui mafic clasts, from this study, Rooyakkers (2015) and Wilson et al. (2006). **a** Plot of FeO^*/MgO versus SiO_2 to show the two compositional groupings (calc-alkaline and tholeiitic: Wilson et al. 2006, dividing line from Miyashiro 1974). **b** New ICP-MS derived values for the Eu/Eu^* ratio (Table 3 and Electronic Appendix 1). Note, in the tholeiitic group in particular, the positive Eu anomalies (i.e. $\text{Eu}/\text{Eu}^* > 1$) of most clasts, indicative of plagioclase accumulation

A common magmatic history can, therefore, be inferred for the majority of plagioclase, orthopyroxene and amphibole crystals in the HSR clasts: derivation from a deeper, hotter and less evolved source mush, followed by entrainment and crystallisation of rim-zones in the cooler, shallower and more evolved melt-dominant magma body. The earlier history of HSR quartz crystals, however, contrasts with that inferred for these other main phases, with the trapped melt inclusions recording more evolved compositions than the final (HSR) melt-dominant magma body. Crystallisation of the quartz rim-zones took place in the melt-dominant magma body, along with plagioclase,

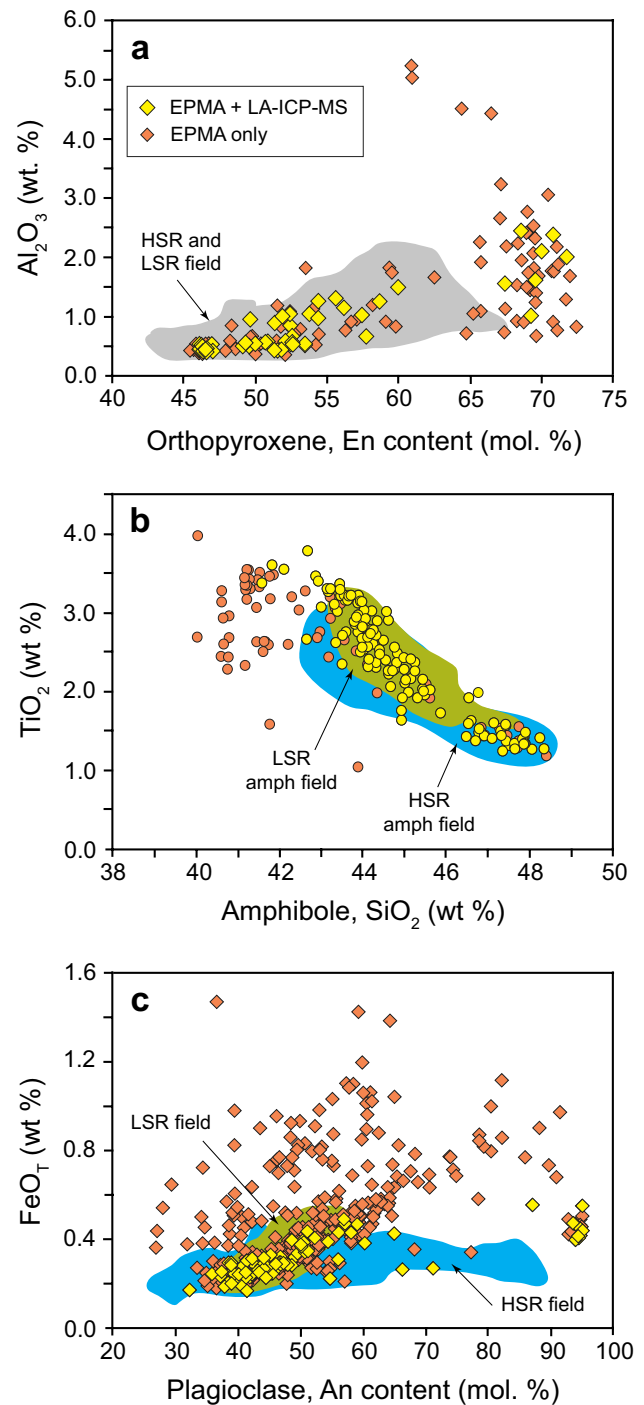


Fig. 8 Comparisons of selected major element compositions of crystals from the mafic versus rhyolitic clasts. The yellow symbols identify analyses for which in situ trace element data are available, whereas the orange symbols show analyses for which there is no corresponding trace element data. The higher spatial resolution of EPMA versus LA-ICP-MS was the main limiting factor in determining which crystals could be analysed for their trace element contents

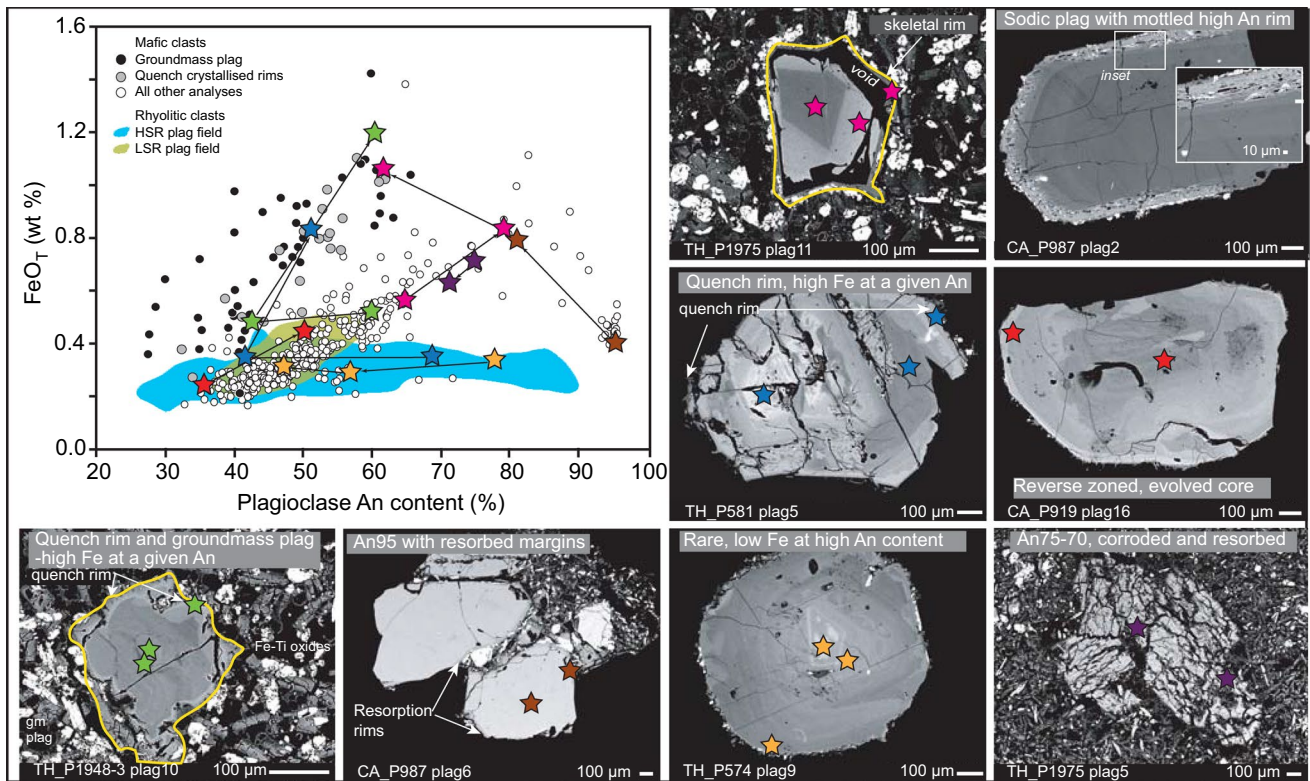


Fig. 9 The textural and compositional linkages between plagioclase crystals in the mafic clasts. BSE images of selected crystals are shown here to highlight some of the linkages that can be made between textures and composition, represented by a plot of FeO_T versus An content. Analysis spot points in the crystal images are marked with coloured stars that correspond to the equivalent coloured symbols in the central plot. The portion of the mafic clast dataset that

plots at higher FeO_T contents at a given value of An (black and grey filled circles) consists entirely of analyses of rapidly grown plagioclase, i.e. flash crystallised microlites in the groundmass and thin, quench-crystallised rims. The illustrated samples are labelled at the bottom of the images with CA and TH denoting crystals from calc-alkaline and tholeiitic clasts, respectively

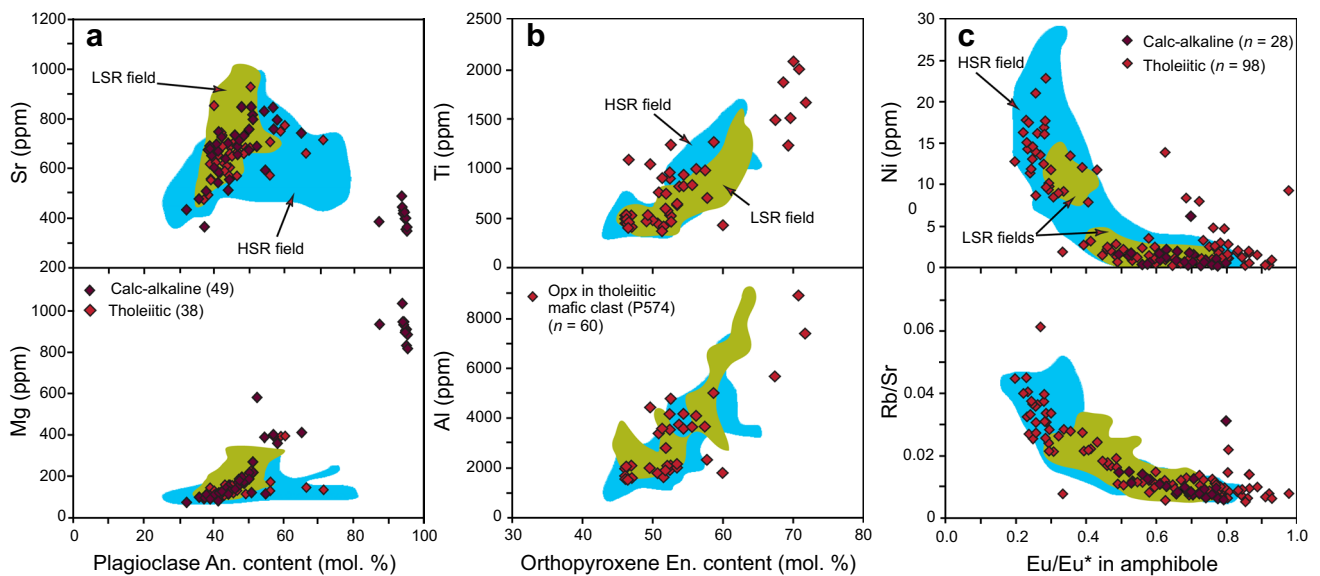


Fig. 10 Selected trace element compositional data of crystals from Oruanui juvenile mafic clasts. **a** Plagioclase. **b** Orthopyroxene from a representative evolved tholeiitic mafic clast (P574; $SiO_2 = 62.4$ wt%). Note: only 35 of the 60 analyses by LA-ICP-MS

on this sample included Al in the analytical scan. **c** Amphibole. The grey shaded regions in all panels show the corresponding compositional ranges from crystals from the HSR (blue) and LSR (green)

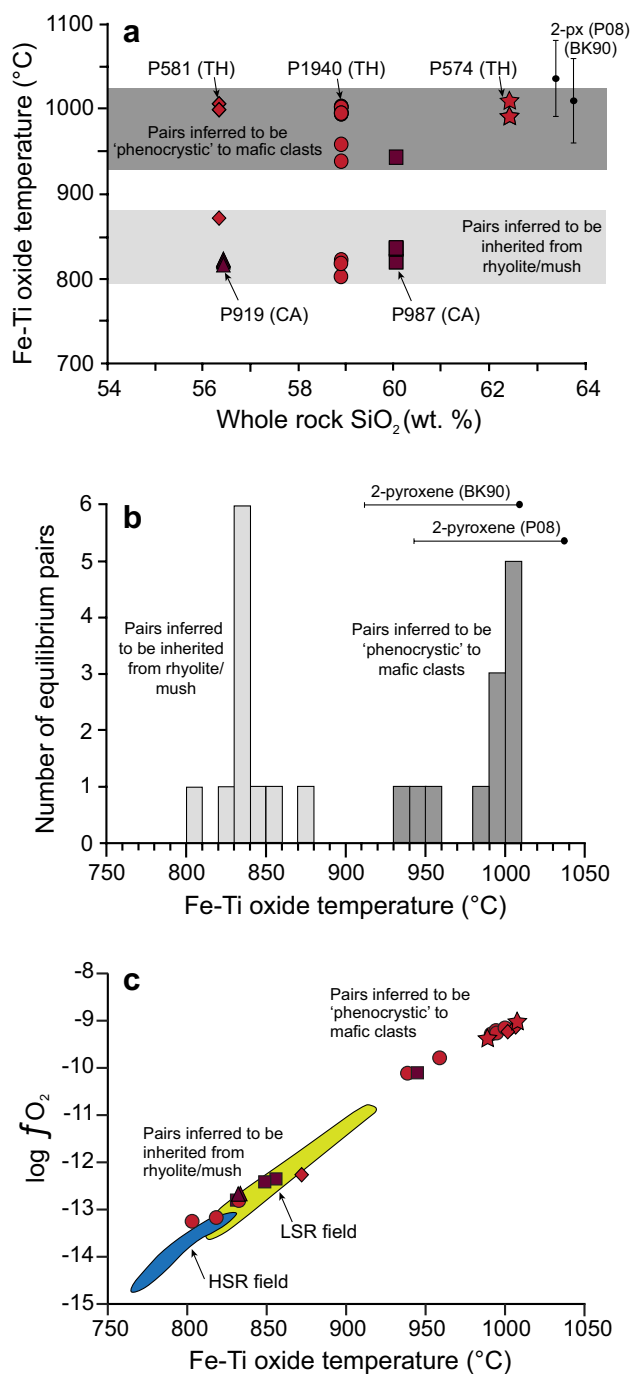


Fig. 11 **a** Fe–Ti oxide temperatures for equilibrium pairs (after Bacon and Hirschmann 1988) extracted from Oruanui juvenile mafic clasts. Temperatures are calculated using the model of Ghiorso and Evans (2008). Note the bimodality of the temperature estimates. The lower temperature group is assumed to represent pairs of oxides that were entrained from the crystal mush pile and/or during interactions with the rhyolite body. **b** Mean (± 2 SD) temperature determinations from two-pyroxene thermometry for 19 equilibrium opx–cpx pairs (i.e. $K_D(\text{Fe–Mg}) = 1.09 \pm 0.14$). BK90—Brey and Kohler (1990); P08—Putirka (2008, his equation 37). **c** Fe–Ti oxide temperatures in the mafic clasts (from **a**) versus oxygen fugacity, with the respective fields for the LSR and HSR plotted

orthopyroxene and amphibole, as shown by the close correspondence between compositions of the host melt (i.e. groundmass glass) and those of re-entrant inclusions (Liu et al. 2006).

Allan et al. (2013) highlighted the significant compositional overlap between the earlier grown portions of the HSR crystals (i.e. cores plus interiors) and whole crystals from the LSR, in addition to overlapping P–T conditions indicated by amphibole compositions. They argued that the LSR magma, seen as discrete clasts ejected during the eruption in only minor proportions, in fact approximated the initial composition of the voluminous crystal-poor magmas extracted from the crystal mush/source zone. The hundreds of cubic kilometres of this magma that were extracted then, following crystallisation of the rim-zones on many crystals and associated cooling of the order of 40–50 °C, culminated in the final HSR composition. This is consistent with the findings of Wilson et al. (2006) that the HSR compositions could be generated from LSR compositions following $\sim 28\%$ fractionation of the crystal phases recorded in the pumices. In this light, the LSR pumices that were sampled during the eruption itself are considered to represent isolated bodies of crystal-poor rhyolite magma that existed in the crystal-mush source reservoir, and that were syn-eruptively tapped during evacuation of the HSR magma body (cf. Cashman and Giordano 2014). Allan et al. (2013) noted that all LSR clasts examined were quartz-free and that quartz may have only begun to grow in the melt-dominant magma body after the melt had evolved to SiO₂-saturated conditions. The short (decades to centuries) timescales proposed from melt inclusion faceting in the Oruanui quartz by Pamukcu et al. (2015) thus only reflect a part of the physical and chemical evolution of the magma body. In light of the expanded crystal-specific dataset considered here, we review these approaches to more fully explain some of the features of quartz and the other crystal phases discussed above.

A revised model for the pre-eruptive development of the Oruanui magma body

The diversity of compositions and inferred P–T conditions determined from the crystal cores and interiors reflect earlier derivation of the crystals from a thermally and compositionally zoned crystal-mush source. During the processes of crystal-liquid separation, large volumes of melt plus entrained crystals were carried upwards into the melt-dominant magma body that was forming at shallow crustal levels (~ 90 – 140 MPa, or ~ 3.5 – 6 km depth). Convection and stirring of the accumulating melt-rich body destroyed any compositional stratification (cf. Bishop Tuff: Hildreth and Wilson 2007; Chamberlain et al. 2015) and resulted

in melt homogenization that generated compositionally uniform crystal rims. Quartz-hosted melt inclusions (indicating crystal growth from more evolved melts during the formation of the crystal interiors, to slightly less evolved conditions in the main melt-dominant magma body: Fig. 4; Liu et al. 2006, also Bégue et al. 2015) indicate that quartz was only stable in the uppermost layers of the mush body prior to melt segregation. The interstitial melt in this part of the mush was highly evolved (on the basis of Rb/Sr ratios) and the modal values from volatile saturation pressures (Liu et al. 2006) indicate that this zone was at pressures of ~120–150 MPa (~4.5–5.5 km depth) but not greater than ~190 MPa (>7 km depth). Compositional characteristics of melt inclusions in sparse CL-dark quartz cores observed by Liu et al. (2006) and age characteristics of inherited zircons in post-Oruanui eruptives (Charlier et al. 2010; Barker et al. 2014) are consistent with at least part of this mush being an intrusive remnant of the 350 ka Whakamaru magma systems (Brown et al. 1998; Matthews et al. 2012). It thus seems likely that some of the plagioclase (e.g. those with compositions notably more evolved than the outermost rims), amphibole and orthopyroxene co-crystallised with quartz in this upper part of the mush layer. Similarly, a small component of the amphibole cores and interiors have low-Al compositions that may reflect their earlier growth and crystallisation from evolved interstitial melt in the quartz-bearing portion of the mush. Quartz is absent in the post-Oruanui rhyolites (Barker et al. 2015), which are typically 20–60 °C hotter than the Oruanui magma, supporting the inference that quartz was only stable in the upper and cooler parts of the pre-Oruanui mush.

Downward thermal and compositional stratification of the mush below the quartz-bearing zone is reflected in the compositions of plagioclase (increasing An content: Fig. 5a–d) and orthopyroxene (increasing En content: Fig. 5e, f). The amphibole compositions reflect increasing model temperatures with depth in the mush pile, reaching ~920 °C at pressures of ~270 MPa or ~10 km depth, with corresponding compositional gradients reflected in co-related Eu/Eu* values (Allan et al. 2013: Fig. 6). In addition, the plagioclase compositional data from the HSR clasts show evidence for two contrasting sources for the An >50 plagioclase cores (Fig. 5). A subordinate population has somewhat depleted concentrations of compatible elements (e.g. Sr, Mg; Fig. 5c) and elevated levels of incompatible elements (e.g. Ba, Pb; Fig. 5d) at values of An >50. Although these particular cores have bulk compositions that are consistent with growth from (qualitatively) hotter and/or drier melts, their trace element characteristics indicate that those melts were comparatively more evolved. In contrast, the dominant population of plagioclase crystals (both cores and rims) show higher Sr, Mg and lower Ba, Pb contents and are thus inferred to have crystallised

from contrasting melts. On the basis of these characteristics we suggest that the high-An, low Sr (and Mg) plagioclase cores grew from melts with a significant (tens of percent) crustal component, although there is a diversity of possible crustal compositions available (Ewart and Stipp 1968; Charlier et al. 2010; Price et al. 2015). In contrast, the low Ba (and Pb) parts of the crystals are inferred to have grown from more broadly intermediate melts, with lower crustal contributions. This inference is in line with evidence from the blue-grey-cored Oruanui plagioclase crystals (Charlier et al. 2008), in which high An overgrowths around the cores were interpreted to have grown from almost ‘pure’ crustal melts with accompanying high $^{87}\text{Sr}/^{86}\text{Sr}$ values (see also Charlier et al. 2010). Such findings not only highlight the wide variety of source melt compositions and the open-system nature of the Oruanui reservoir, but also a heterogeneity of crustal sources and degrees of assimilation within different regions of the pre-eruptive mush body.

The role of mafic magma in the Oruanui eruption

In applications of the crystal mush model to the development of eruptible material, importance is often placed on the role that mafic magmas play in providing heat and volatiles to defrost and remobilise the mush (e.g. Bachmann and Bergantz 2006; Burgisser and Bergantz 2011; Huber et al. 2011; Karlstrom et al. 2012; Parmigiani et al. 2014; Bachmann and Huber 2016). Elevated rates of mafic intrusion have also been suggested as a mechanism for pre-eruptive heating and priming in post-Oruanui eruptions from Taupo (Barker et al. 2016). The involvement of two distinct, mafic magmas in the Oruanui eruption, therefore, raises questions as to what role these mafic magmas had in mush reactivation or initiating the eruption. The estimated total volume of mafic magma erupted (~3–5 km³) is significantly larger than any other known eruption of purely mafic material in the TVZ (Wilson 2001). However, the ubiquitous down-temperature signatures in the rim-zones of the main crystal phases in the HSR (e.g. decreasing An in plagioclase, decreasing En in orthopyroxene) preclude the notion that injection of mafic material triggered the eruption through mafic recharge-driven heating (Fig. 5; cf. Barker et al. 2016). Wilson et al. (2006) suggested that some tholeiitic mafic magma may have ponded at the base of the primed Oruanui melt-dominant magma body in the weeks to months prior to eruption, and this is supported by evidence presented here for interaction between tholeiitic magma and the LSR and (but to a lesser extent) HSR magmas (Figs. 12, 13). The resulting convection and stirring brought about by the hot mafic floor to the melt-dominant magma body was used by Wilson et al. (2006) to explain the homogenisation of any significant pre-existing compositional zonation. Here, we consider how such processes

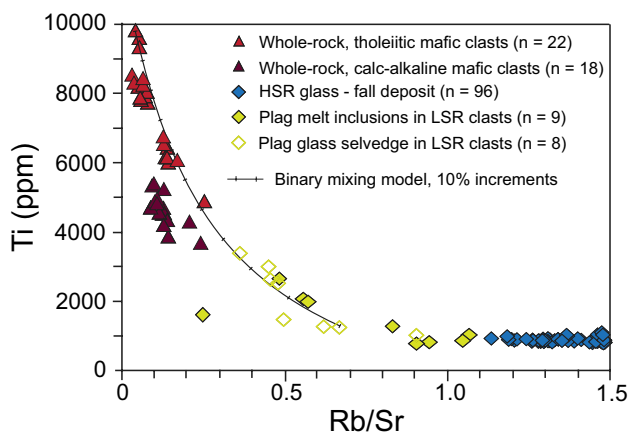


Fig. 12 Ti versus Rb/Sr data for rhyolitic glasses (as annotated) and juvenile mafic clasts (whole-rock). The steeper trend observed in the LSR plagioclase selvage and melt inclusion data are taken as indicating involvement of the tholeiitic mafic magma with the LSR glasses, and mixing controls on the tholeiitic whole-rock variations being with melts in the mush zone, not the melt-dominant body

would be reflected in the zonation of minerals and in the textures in the mafic clasts.

Chemical analysis of the macroscopic crystals from individual mafic clasts (Fig. 8, Fig. S.4) shows that many of these crystals are identical in composition to those found in HSR and LSR clasts and hence inferred to be inherited. The positive Eu/Eu^* values in almost all of the tholeiitic clasts (Fig. 7) are also indicative that this magma has accumulated or assimilated significant amounts of plagioclase. One of the two trends observed in the trace element glass compositions of LSR plagioclase-melt inclusions and selvages (Fig. 2b) can be explained by binary mixing between LSR compositions and the least evolved tholeiitic magma (Fig. 12). Trends within the mafic whole-rock data can be revisited in the light of the inference that the mafic magmas accumulated a significant component of ‘rhyolitic’ crystals. Three similar but subtly different trends are highlighted within the tholeiitic clasts (Fig. 13) suggesting that the overall tholeiitic group itself may comprise at

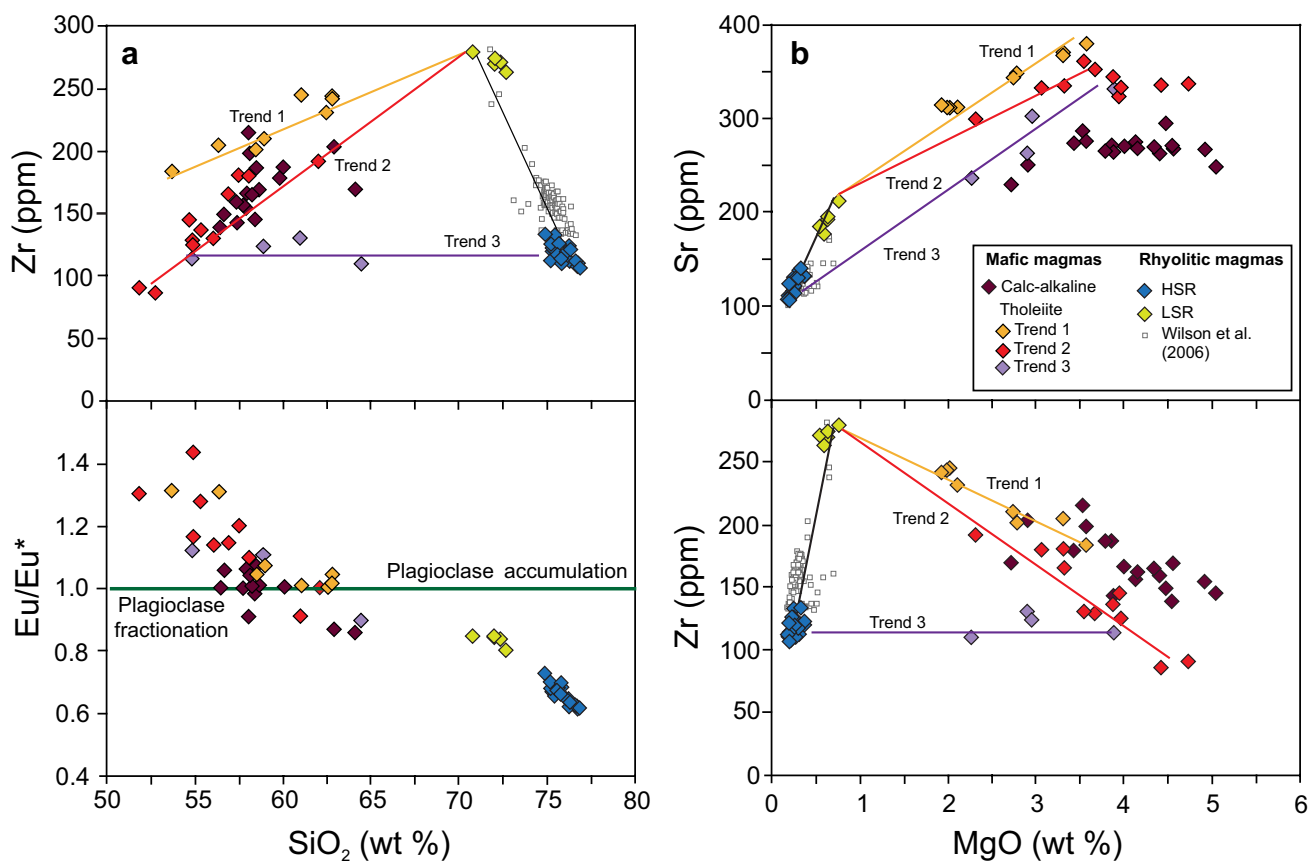


Fig. 13 Selected whole-rock analytical data for Oruanui felsic and mafic clasts. The tholeiitic group is split into three sub-groups on the basis of possible mixing trends. Chemical trends in the mafic groups

overwhelmingly trend towards the LSR compositions and only 3 clasts (‘trend 3’) plausibly trend towards the volumetrically dominant HSR compositions

least three discrete batches of magma. The overall patterns within the whole rock data trend towards LSR compositions, with the exception of trend 3 in Fig. 13 (four samples) that plots on a compositional trajectory towards HSR compositions. The whole-rock compositional trends within the mafic magma suites, particularly the tholeiitic group, and the apparent mixing trend seen in the glass data of LSR samples indicate that some mafic magma interacted with rhyolitic compositions for an extended period before the clasts were quenched or the eruption commenced.

In addition, a particular feature of the amphibole trace element data is the unusual increase in Ni and Co abundances with decreasing Eu/Eu* and model crystallisation pressure (Fig. 6c, d). These two elements occur at very low levels in the HSR rhyolite in general (Table 2), although the MgO-enriched pumices reported by Wilson et al. (2006; see Table 1) also have slightly enhanced levels of Ni and Co, barely discernible in their XRF data. Similar results to those of Wilson et al. (2006) were reported by Kaneko et al. (2015), also from whole-rock XRF data. Mafic recharge is unlikely, however, to have caused the increased Ni and Co levels widely distributed in the amphiboles (i.e. those crystals from HSR pumices that do not show higher MgO values) because the HSR amphiboles (plus orthopyroxene and plagioclase) all are zoned outwards to compositions reflecting cooler and more evolved melt compositions. We infer that the elevated amphibole Ni and Co levels reflect the dissolution of a high Ni–Co phase into the HSR magma, with these elements then being sequestered into the amphiboles. Of the other crystal phases in the Oruanui eruptives only the Fo₈₅ olivines found in the calc-alkaline mafic magmas are strongly enriched in these elements (Ni ~750 ppm; Co ~180 ppm; Electronic Appendix 8). We infer that at some pre-eruptive stage(s), olivine-bearing, relatively primitive mafic magma reached either the melt-dominant body or the upper, evolved levels of the crystal mush zone and the olivines reacted out. Due to the relatively low levels of other trace elements in these olivines (see Electronic Appendix 8), their dissolution into a large rhyolitic magma body would leave little trace, with Fe–Mg contents being readily taken into ferromagnesian minerals in the rhyolitic assemblage or slightly increasing the MgO content of a small fraction of the HSR. The elevated Ni and Co contents in the HSR amphibole rims may thus be cryptic evidence for a role olivine-bearing (i.e. calc-alkaline) mafic magma in the earlier assembly of the Oruanui melt-dominant magma body than can be inferred from any other information at present.

Diffusive timescales in the Oruanui magmatic system

Elemental diffusion in volcanic crystals can be used to provide information about the timescales of sub-surface

processes (Costa et al. 2008, for review), and here we highlight three mineral species in particular to place a range of temporal constraints on pre- and syn-eruptive processes in the Oruanui magmatic system.

Fe–Mg diffusion timescales in orthopyroxene

Within the Oruanui magmas pre-eruptive timescales on the order of decades to millennia have been obtained from modelling of Fe–Mg diffusion in orthopyroxenes. Allan et al. (2013) modelled the prominent main core–rim boundaries in HSR orthopyroxenes (Fig. 3a), a feature that they interpreted to represent the physical arrival of individual orthopyroxene crystals along with their host LSR melt from the underlying mush into the growing melt-dominant magma body. With allowance for maximum uncertainties in model parameters (especially temperature and oxygen fugacity; Chamberlain et al. 2014a), it was inferred that the crystal–liquid segregation process that led to the generation of the melt-dominant magma body did not begin until only ~1600 years prior to the eruption, consistent with previous inferences from zircon model-age spectra (Wilson and Charlier 2009). Probability density function analysis indicated that the peak ‘extraction age’ was ~230 years earlier and that there was an apparent period of stasis ~60 years just before the eruption.

With revisions to magmatic temperatures (Barker et al. 2015; this paper) and the publication of a new model for Fe–Mg interdiffusion in magnesian orthopyroxene (Dohmen et al. 2016), we have revisited the timescale estimates of Allan et al. (2013). An extended discussion is given in the supplementary material, but the various changes to parameters (Table S.5), combined with the correction of a numerical error, leads to a reduction in timescales of a factor of three (Fig. S.6). This migrates the peak extraction time to 80 years pre-eruption with the inferred pre-eruption stasis period of 20 years (Figs. S.7 and S.8) but does not substantively change the conclusion that mobilisation is geologically rapid, and by implication involving the upwards transport of >1 km³/year of magma). These timescales are similar to those proposed from the faceting of Oruanui quartz-hosted melt inclusions (Pamukcu et al. 2015), and both timescales may reflect the same process of rapid assembly of the melt-dominant body, although the mineral species concerned come from different domains within the mush.

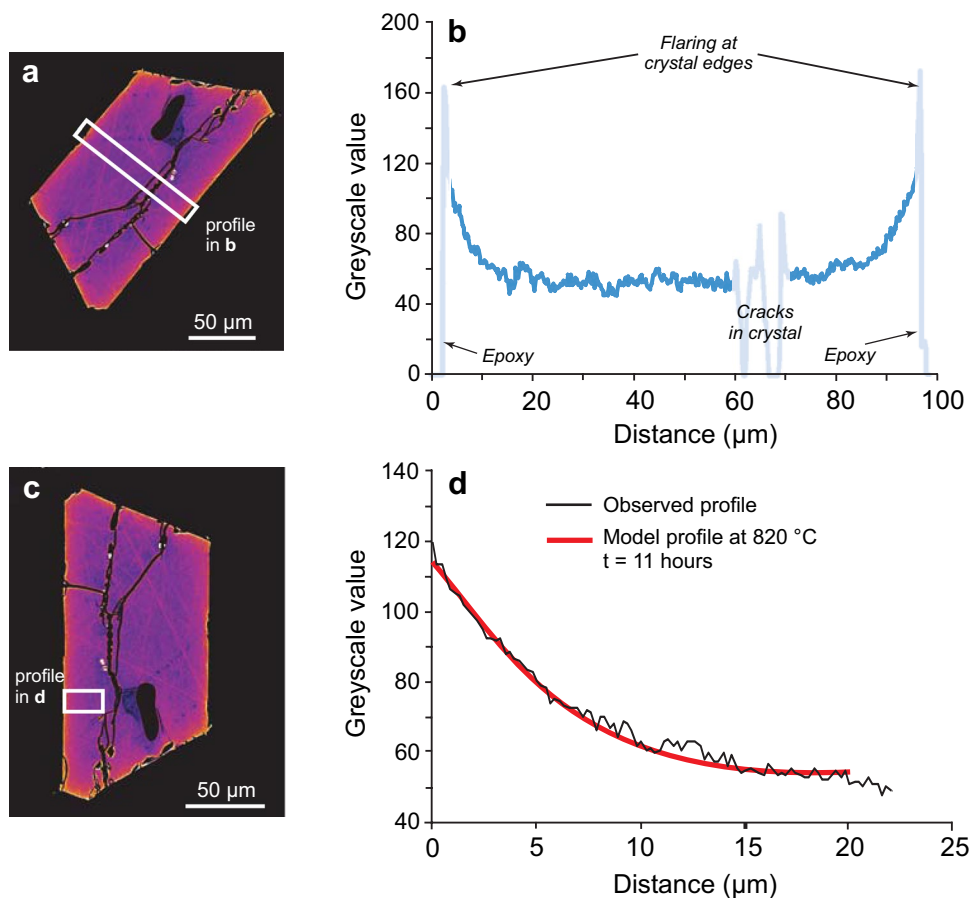
Fe–Ti diffusion timescales from magnetite

BSE imagery of Fe–Ti oxide crystals extracted from the mafic clasts shows that many magnetite crystals in these samples are compositionally zoned (Figs. 14 and S.9). Fe–Ti oxides, and magnetite in particular, are known to rapidly

re-equilibrate in response to fluctuations in magmatic conditions (Freer and Hauptman 1978; Aragon et al. 1984; Nakamura 1995; Venezky and Rutherford 1999; Coombs et al. 2000; Devine et al. 2003). The preservation of Fe–Ti zonation in magnetites in the Oruanui mafic clasts, therefore, is taken as a record of a process (or processes) operating shortly before quenching on eruption. Using *ImageJ* (<http://rsb.info.nih.gov/ij/>), we retrieved spatially resolved transects across the BSE images and compared them to the chemical composition along the same transects as measured by EPMA (e.g. Fig. 14). The greyscale values from the BSE images strongly reflected changes in the Fe–Ti content of the magnetite. Although zonation in some minor element oxides was also evident (e.g. Al_2O_3 and MgO), variations in the concentrations of these elements appeared to have little or no influence over the greyscale zonation, allowing the BSE intensity to be calibrated for Ti content. Using the changing greyscale intensity to infer the changing Fe–Ti contents of the zoned crystals, we used the BSE images to recover information about Fe–Ti zonation at a higher spatial resolution than that possible by direct EPMA spot analyses. We modelled Fe–Ti interdiffusion in magnetite crystals to calculate the timescale(s) over which mafic-felsic mingling occurred prior to quenching upon eruption

(Fig. 14). To determine the magnetite Fe–Ti diffusion coefficient in the Oruanui system, we used the experimentally derived parameters of Aragon et al. (1984), and conducted our modelling at conditions of 820 °C and an oxygen fugacity of NNO. These conditions correspond to the lowest temperatures and oxygen fugacity conditions inferred from the cores of equilibrium Fe–Ti oxide pairings within the mafic clasts (Fig. 11) and should yield a maximum estimate. On this basis, the timescales obtained are between 6.7 and 37 h ($n = 18$), but mostly <18 h, and are interpreted to reflect syn-eruptive mixing processes prior to quenching at the surface. Alternative modelling using diffusivity from Freer and Hauptmann (1978) at the same conditions of T and $f\text{O}_2$ yields timescales a factor of ~3 shorter than the Aragon et al. (1984) formulation, but this does not change the conclusion that the Fe–Ti oxide crystals record magma mixing processes occurring just hours before the magma was quenched. The samples used for modelling were from pumices in phase 7 ignimbrite, the coeval powerfully dispersed fall unit of which contains the greatest proportions of mafic material (up to 4% of the juvenile fraction: Wilson 2001). Fall deposits of phases 6 and 7 are separated by a short time gap during which the eruption plume fully dissipated, but no erosion occurred (Wilson 2001). These

Fig. 14 An example of a Fe–Ti diffusion modelling of a zoned magnetite crystal from clast P987 (calc-alkaline). In **a**, **b** the greyscale zonation across the crystal is examined to check for symmetry of the profile. Note the ‘flaring’ effect at the very edges of the crystal. In **c** a higher resolution portion of the crystal is selected for modelling, and in **d** a model curve is fitted to the observed profile. In this example the crystal is interpreted to record a thermal perturbation in the final ~11 h prior to quenching on eruption



factors suggest that the Fe–Ti oxide zonation reported here is recording syn-eruptive timescales related to inputs of fresh mafic magma during the time break between eruption phases 6 and 7.

Fe–Mg diffusion timescales from olivine

Despite the abundance of olivine in the calc-alkaline mafic clasts, very few crystals were suitable for Fe–Mg diffusion modelling. All of the large (1–2 mm) olivine crystals in the calc-alkaline samples have very thin (<5 μm) bright rims in the BSE images reflecting a higher Fe-content. However, closer inspection of the greyscale zonation patterns of the rims (which correlate directly to the changes in the Fe–Mg content of the olivine, e.g. Martin et al. 2008) suggests that these zonation features are not solely diffusion controlled, but reflect a quench crystallisation/growth feature of the olivines accompanying mafic-felsic interaction, indicated by regions of linear compositional gradient in the crystal rim and the lack of a single rim plateau value. Although the rim zonation was not suitable for more rigorous Fe–Mg diffusion modelling, examination of the interaction between the homogeneous cores and the growing rim-zone does impart some constraints. Typically we see a very abrupt change between the core and the steadily increasing rim, with only a very narrow region of curvature between the two, which would be the natural consequence of diffusion. Based on the uniformly small length scales of these regions (<5 μm), we can estimate a maximum timescale over which these regions of abrupt curvature could be preserved. Based on a temperature of ~ 820 °C and NNO oxygen fugacity, the olivine rim zonations are consistent with an event that occurred at most no more than a few weeks before quenching, consistent with short timescales inferred from experimental studies on olivine mixing with silicic melts (e.g. Coombs and Gardner 2004). Although more rigorous constraints are not available we suggest that it is possible that the quench rims on the olivines formed during the same event recorded by the zoned magnetite crystals.

A cascade of events and their associated timescales as inferred from the Oruanui crystal archive

By combining our new results with previously published studies, an overview of the cascading timescales of pre- and syn-eruptive processes culminating in the Oruanui eruption is presented (Fig. 15). From these studies, it is clear that the overall history of the magmatic system that gave rise to the Oruanui eruption (and its precursory leaks: Sutton et al. 1995; Wilson and Charlier 2009) is not encapsulated in any one crystal phase or manifested on any one timescale.

At one extreme, the timescale for the growth of the Oruanui mush zone, with its distinctive chemical and isotopic compositional characteristics and zircon model-age spectra goes back around 40 kyr (Sutton et al. 1995; Wilson et al. 2006; Wilson and Charlier 2009). A model that used Oruanui zircon model ages (Wilson and Charlier 2009) in isolation to infer a magma chamber lifetime of 200 kyr (Caricchi et al. 2014b) is flawed, for three reasons. First, the model-age spectrum used only represents those grains (or parts thereof) that yielded model ages 1 SD or more below the equiline in the U–Th disequilibrium system. The earliest ages presented in Wilson and Charlier (2009) are thus not indicative of the oldest ages present in the zircon suite. Second, a given age estimate from part of a zircon gives no indication in itself as to whether that age reflects material that is foreign and inherited through recycling (xenocrystic; cf. Charlier et al. 2005, 2010; Barker et al. 2014), consanguineous and inherited (antecrystic), or phenocrystic and growing in the magma body that actually erupted. There is thus no single zircon age determination (regardless of its precision) that can be uniquely defined as representing the onset of the Oruanui magmatic system. Third, during the ~ 200 kyr period prior to the Oruanui event, large volumes of volcanic products attest to the presence of compositionally unrelated magma systems (such as the NE dome system) active in the Taupo area (Sutton et al. 1995; Leonard et al. 2010; Cattell et al. 2016). The onset of the Oruanui magma system in terms of surface eruptives is around 60 ka (Sutton et al. 1995), and the commonality of a ~ 86 –96 ka peak in zircon model ages for the Oruanui and earlier geochemically linked rhyolites (Charlier et al. 2005; Wilson and Charlier 2009) suggests a common source that experienced an enhanced episode of cooling and crystallisation at that time. The dominant younger peak of zircon model ages in the Oruanui magma (37–41 ka across three samples: Wilson and Charlier 2009) also represents a peak crystallisation in prior to formation of the Oruanui melt-dominant body at a time when surface volcanism was inactive in the Taupo area (Wilson et al. 2009).

Extraction of melt plus entrained crystals to form the melt-dominant body only occurred within the ~ 3000 year time gap between the Oruanui (25.4 ka) and its precursor Okaia event at 28.6 ka from a geographically overlapping vent (Allan et al. 2013; Lowe et al. 2013) on the basis of the greatly contrasting zircon model-age spectra between the two suites of products (Charlier et al. 2005; Wilson and Charlier 2009). This time gap is only bracketed by the zircon data, but quantified in detail by the textural information and diffusion-profile model age information from Oruanui pyroxenes to have been mostly accomplished in decades to centuries (Allan et al. 2013; this paper). Faceting of quartz-hosted melt inclusions (that were avoided in the work by Liu et al. 2006) also suggests a centennial timescale for

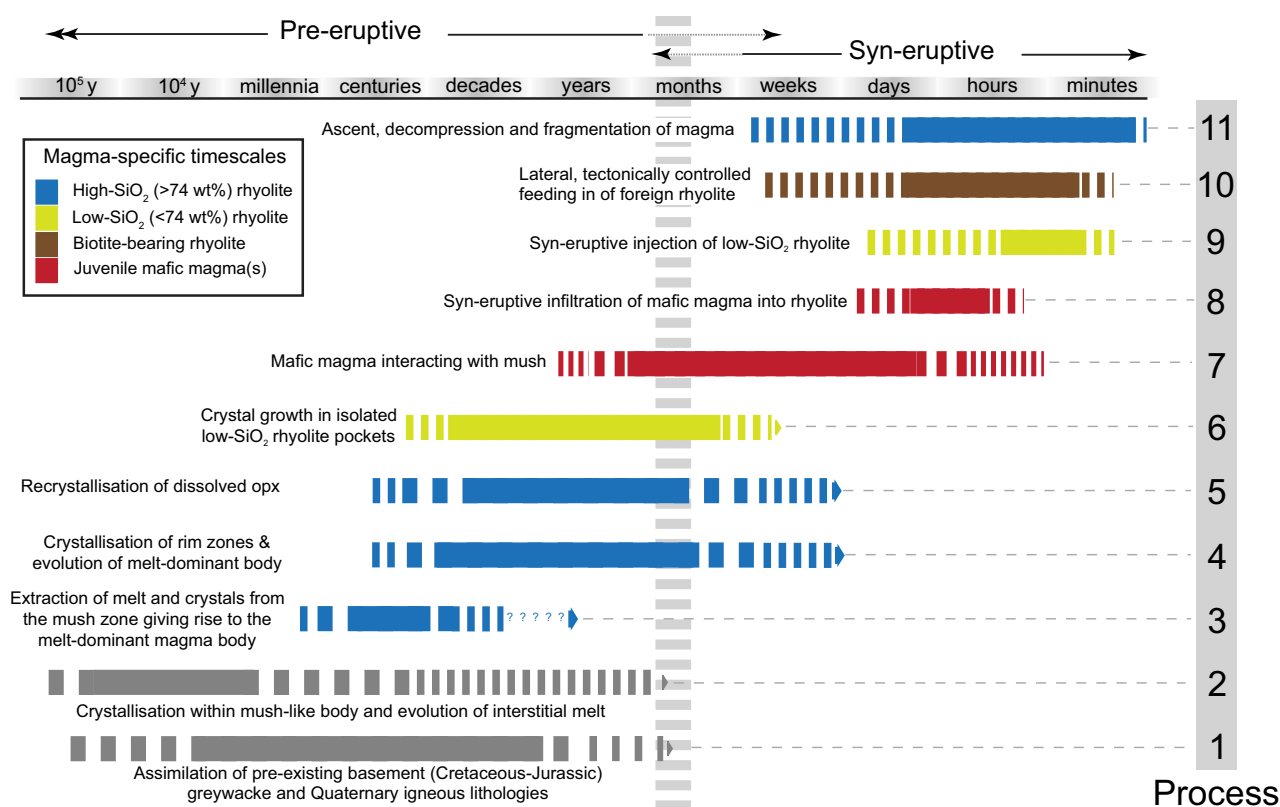


Fig. 15 Summary figure to show the timescales of processes involved in the generation, accumulation and destruction of the Oruanui magma body as inferred from combined crystal-specific and field studies. Processes are numbered as follows. 1 Compositional characteristic of melt inclusions in xenocrystic quartz cores (Liu et al. 2006), radiogenic fingerprinting of xenocrystic blue-grey-cored plagioclase (Charlier et al. 2008), U–Pb zircon age fingerprinting of ‘old’ zircons (Charlier et al. 2010). 2 U–Th age spectra of zircons and crystal inheritance patterns with Oruanui precursor eruptions (Charlier et al. 2005; Wilson and Charlier 2009). 3 Processes identified by reconciliation of textural, thermobarometric and compositional data from orthopyroxene and amphibole (Allan et al. 2013). Timescales constrained as outlined in point 4 and in the supplementary material.

4 Fe–Mg diffusion timescales across the main core–rim boundaries in orthopyroxene (Allan et al. 2013). The equivalent boundary is texturally observed in plagioclase (this paper and Charlier et al. 2008). 5 Fe–Mg diffusion timescales from re-crystallised streaky, discontinuous zones in orthopyroxene (Allan et al. 2013). 6 Fe–Mg diffusion timescales from growth zones in orthopyroxene (Allan et al. 2013). 7 Crystal inheritance pathways, textural observation and disequilibrium textures (this paper). 8 Fe–Ti diffusion timescales in magnetite crystals (this paper). 9 Compositional relationships in matrix glass and crystals (this paper). 10 Compositional source fingerprinting and field constraints (Allan et al. 2012). 11 Li diffusion timescales in plagioclase and quartz (Charlier et al. 2012) and H₂O and CO₂ diffusion timescales from melt pockets (Liu et al. 2007)

the lifetime of quartz growth in the melt-dominant body (Pamukcu et al. 2015).

Over years to days, interactions between the mafic and rhyolitic magmas are likely to become important. In many examples globally it has been inferred that injection of mafic magma into a body of evolved magma may precede eruption by days to months (e.g. Sparks et al. 1977; Pallister et al. 1992; Snyder 2000; Leonard et al. 2002). In the case of the Oruanui, however, evidence from the deposits of phases 1 and 2 also implies strongly that external tectonic forces played a central role in starting and modulating the eruption during these phases over comparable time periods (Allan et al. 2012). The evidence for the ‘foreign’ NE dome-type rhyolitic magma migrating at shallow levels into the Oruanui conduit again implies strongly that the

onset and initial stages of the eruption were not controlled by properties (overpressure, volatile saturation, etc.) intrinsic to the magma chamber itself (cf. Blake 1984; Foroozan et al. 2011; Gregg et al. 2012). What remains uncertain is whether the large volumes of mafic magmas involved in the Oruanui eruption were opportunistic in exploiting a changing stress field to rise into the mush zone and base of the melt-dominant body, or whether the mafic magmas were active participants in controlling the crustal stress field (Rowland et al. 2010). Evidence given above implies that some mafic magmas interacted with the mush zone or the melt-dominant body prior to the eruption and that multiple batches of magma were involved. However, these interactions were not to an extent that led to any widespread heating signal in the compositions of crystals growing in the

melt-dominant body and thus were at best, minor. Later in the eruption sequence, diffusive time estimates from Fe–Ti oxides suggest that the sharply defined onset of phase 7 coincided with intra-eruptive injection of a batch of mafic magma. Such injections resulted in enhanced juvenile mafic proportions, and may have also contributed to the marked escalations of eruptive vigour into phases 3 (when LSR clasts also peak in abundance), 7 and 9 (Wilson 2001).

At the other extreme, the shortest timescales that can be quantified here are limited by the ability of eruption products to preserve changing conditions in the crystal record. For the Oruanui eruption, the limits are in those timescales that are captured by fast-diffusing elements or species that can react to changes in physical conditions associated with magma rise during eruptive activity. Water and CO₂ gradients in melt pockets in quartz (Liu et al. 2007) record rise rates of 5–35 cm/s as the magma started to actively vesiculate, and Li gradients in quartz and feldspar record transient processes as the magma ascended at metres to tens of metres per second (Charlier et al. 2012).

Magmatism at Taupo: typical or unique for large silicic systems?

Hildreth and Wilson (2007) put forward a model for the Bishop Tuff magma chamber in which gradients in melt chemistry, crystal content and temperature were established and maintained through incremental accumulation from a source mush reservoir. Subsequent work on mineral-specific aspects of the Bishop record has reinforced that concept (Chamberlain et al. 2015; Evans et al. 2016). This model is broadly similar to that for the Oruanui proposed by Allan et al. (2013) and re-emphasised here. However, several features of the two deposits are in stark contrast to one another. For example, the Bishop Tuff magma was compositionally zoned at the time of eruption such that first erupted compositions were the most evolved, while less evolved and more crystal-rich compositions became more prominent as the eruption progressed (Hildreth 1979; Hildreth and Wilson 2007). There thus cannot have been significant large-scale convection operating in the Bishop magma chamber. In contrast, the Oruanui magma, although compositionally diverse, was not zoned in any systematic way (Fig. S.1). This feature and the diversity of mineral and melt inclusion compositions and textures in any one clast (Liu et al. 2006; Wilson et al. 2006, 2012; Wilson and Charlier 2009; this paper) imply that the Oruanui magma body was vigorously convecting.

Early-erupted crystals in the Bishop magma lack prominent zonation and lack evidence for any significant and widespread dissolution/disequilibrium features (Hildreth 1979; Chamberlain et al. 2015), leading Hildreth (1979) to conclude that the Bishop Tuff magma underwent largely

in situ crystallisation and that the crystal cargo was phenocrystic (in the sense used in this paper). Later erupted Bishop crystals do, however, show evidence for influx of a contrasting magma, growth of compositionally contrasting rims on quartz, feldspar and zircons, and introduction of pyroxenes (Peppard et al. 2001; Wark et al. 2007; Reid et al. 2011; Gualda et al. 2012a; Chamberlain et al. 2014a, b, 2015; Gualda and Sutton 2016). Oruanui HSR crystals often have two, readily identifiable and distinct periods of growth. In the orthopyroxene and plagioclase, the earlier and later histories are readily distinguished on the basis of resorption horizons ± sieved texturing or patchy zonation in the cores (Fig. 3), features which are absent in the crystals of the Bishop Tuff. The earlier growth stage is inferred to have occurred within the thermally and compositionally zoned mush body, and the other is reflected in the rim-zones crystallised within the melt-dominant magma body. This melt-dominant body, stirred by convective mixing, also evolved over time (decades), as seen in the decreases in An proportions in plagioclase rims to An₃₈ and En in the orthopyroxene rims to En₄₆.

The question then arises that if both magma bodies accumulated following broadly similar mechanisms, what factors led to the strongly contrasting characteristics of the melt-dominant magma bodies and their crystal cargoes? We suggest that the answer lies in the process(es) that ultimately drive the crystal–liquid segregation and the rates at which large-scale melt extraction processes take place. In the Oruanui, physical extraction from the mush and assembly of the melt-dominant magma body was extremely rapid, at rates exceeding >1 km³/year (Wilson and Charlier 2009; Allan et al. 2013; this paper). Similarly rapid rates of melt extraction have also been demonstrated to have occurred prior to younger eruptions from Taupo (Barker et al. 2016). Allan et al. (2013) suggested that magma-assisted rifting processes prior to the Oruanui eruption may have acted to enhance the melt extraction process by creating gashes through the mush body that acted as focussing channels for melt (and crystals) to migrate upwards and accumulate, as compared with more passive processes (e.g. hindered settling, gas filter pressing) that are generally assumed to drive melt extraction (Bachmann and Huber 2016 for overview). The vigour with which melt and crystals from contrasting compositions, depths and temperatures were brought together in the shallow crustal holding chamber, and the inferred heat loss associated with the 40–50 °C cooling (Allan et al. 2013; this paper), likely resulted in convection and stirring that acted to destroy any chamber-wide compositional and thermal gradients during formation of the melt-dominant magma body. Any early increments of mafic magma that reached the floor of the melt-dominant body may also have served to intensify the mixing processes through providing a source of heat and volatiles (e.g.

Sparks et al. 1984). However, such increments were not big enough in volume to counteract the overall cooling of the melt-dominant HSR body, as reflected in the ubiquitous down-temperature signals in compositions of the major crystal phases.

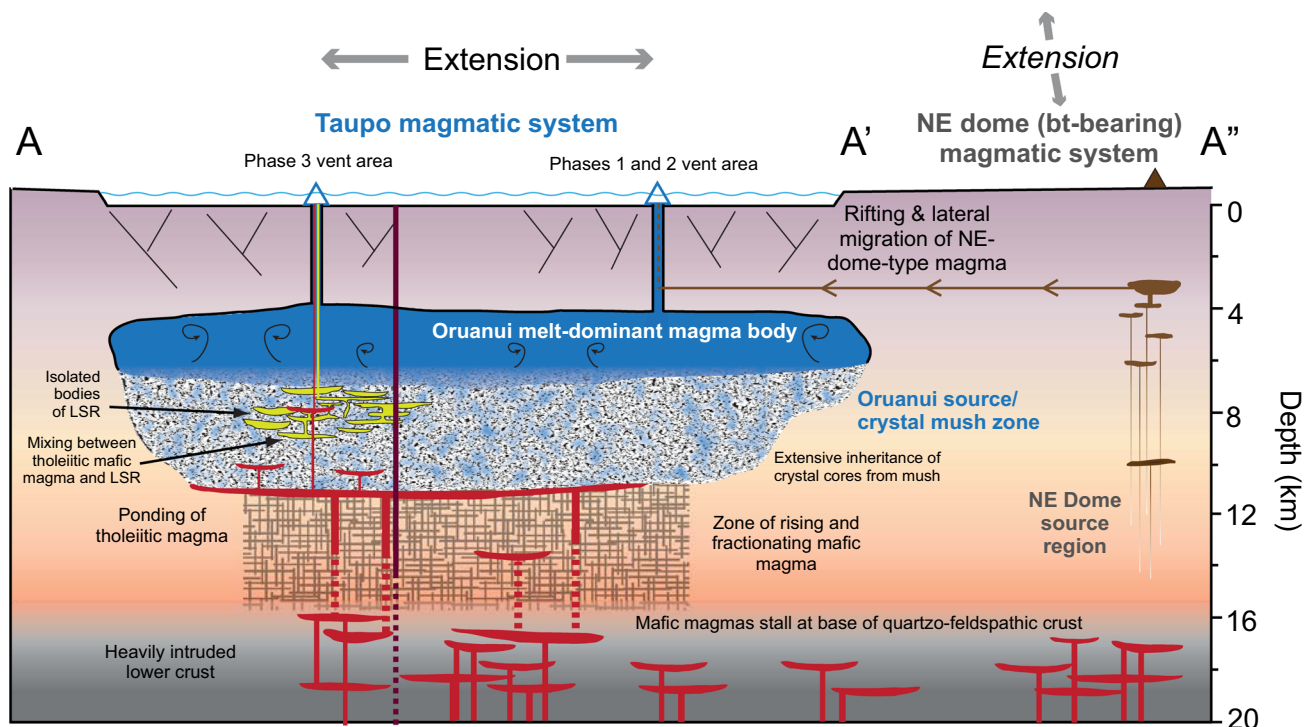
In contrast, no mineral textures that could represent the contrasts between growth in the crystal-dominant mush versus that in the melt-dominant body above have been clearly identified in the Bishop eruption products (particularly the early-erupted material). A maximum timescale for accumulation of the Bishop melt-dominant body has been suggested as 70–80 kyr based on zircon textural and age relationships (Chamberlain et al. 2014b). Much shorter timescales proposed from diffusive profiling across zonation boundaries in quartz (Gualda et al. 2012a; Gualda and Sutton 2016) and melt inclusion faceting (Pamukcu et al. 2015) are interpreted to reflect only the later stages of mixing events that gave rise to zoned crystals (quartz, sanidine, zircon) in the later erupted, deeper derived parts of the melt-dominant body (Chamberlain et al. 2014a, 2015). It seems necessary that to maintain the apparent equilibrium relationships between crystals and melt, and the vertical compositional and thermal stratification, the fluid dynamical processes involved in the melt-dominant magma bodies must have been much more sluggish in the Bishop than the Oruanui.

Identifying minerals, or portions thereof, as phenocrystic, antecrystic or xenocrystic in the Oruanui pumices is challenging. The clearest xenocrystic components are older zircons found as whole grains or cores, and identifiable as such from their age spectra (Charlier et al. 2005, 2010), quartz cores with contrasting entrapped melt inclusion compositions (Liu et al. 2006) and cloudy feldspar cores with contrasting Sr-isotopic systematics (Charlier et al. 2008). The sieve-textured or resorbed cores in the Oruanui HSR plagioclase and orthopyroxenes (Fig. 3) could be characterised as antecrystic, with the interiors having grown in a parental, mush-like reservoir that was, however, physically, compositionally and temporally distinct from the melt-dominant magma body that ultimately erupted. The zircons defining the ~95 and 41–37 ka model-age peaks in the Oruanui and its precursor eruptions are also antecrystic on this basis. The phenocryst population, *sensu stricto*, present in the Oruanui pumices is thus quite restricted. It includes the rim-zones of those crystals (quartz, feldspar, orthopyroxene) that have resorbed or non-equilibrium cores, together with the sparse grains of the same minerals that have homogeneous textures and compositions appropriate to the melt-dominant body (e.g. crystallisation model temperatures diminishing from ~840 to ~790 °C). The Fe–Ti oxides are phenocrystic, regardless of their antecedents, because any inheritance patterns are erased by rapid diffusion. The Fe–Ti oxides, therefore, remained in equilibrium with

conditions in the melt-dominant body (and the rim compositions of other crystal phases) for all except the shortest timescales (hours to days) associated with syn-eruptive magma mixing (Fig. 14). Amphiboles include antecrystic cores and phenocrystic rims (plus subordinate phenocrystic grains), but these are only identifiable by chemical analysis, particularly of trace elements (Figs. 6 and S.5), and are not distinguishable on a textural basis. The bulk crystal population in the Oruanui system is thus not amenable to equilibrium modelling (cf. Bégué et al. 2014) as the majority of the crystal mass is inherited and the host-melt temperature decreases rapidly, with corresponding changes in the outwards crystallising compositions.

Wilson et al. (2006) presented a scaled, schematic cross section of the Oruanui magmatic system immediately prior to eruption. This cross section is revised and updated here in Fig. 16 in light of new details from Allan et al. (2012, 2013) and the findings of this study. Integration of the existing information and new datasets presented here highlight the following details:

1. The realisation that tectonic rifting-related processes played an integral part in triggering the onset of the Oruanui eruption. A body of biotite-bearing rhyolite magma was present in the shallow crust beneath the NE dome system (Figs. 1, 16; Sutton et al. 1995; Wilson and Charlier 2009). Syn-eruptive rifting processes resulted in the southerly propagation of NE dome-type rhyolite magma laterally, to intercept Oruanui HSR magma in the conduit during phases 1 and 2 of the eruption (Allan et al. 2012). Comparable tectonic controls may well have been important in other large, caldera-forming events (e.g. Myers et al. 2016), but the evidence more subtle and not involving magmas of obviously contrasting visible or compositional characteristics.
2. The approximate depth to the top of the melt-dominant magma body. Although similar to that proposed from volatile data (Liu et al. 2006), newer data suggest that its top may have been slightly shallower and lay between ~3.5 and 6.0 km depth (~90–140 MPa). These dimensions, inferred from thermobarometry applied to the outermost rims of amphibole crystals in the HSR, are consistent with the lack of thermal and compositional gradient within the body, and consistent with it being contained within Wilson's (2001) areas 'A' (the structural caldera collapse area) and 'B' (the collapse collar: terms after Lipman 1997) of the Oruanui caldera (Fig. 1).
3. Recognition of the crystal diversity and a range of potential source regions. Approximately 90% of the crystal cargo in the HSR is inferred to have cores and interior domains that were inherited from a stratified



Specific Oruanui magma types

HSR: whole-rock >74 wt% SiO₂

- forms great bulk (98-99%) of magma that is erupted
- compositionally and thermally not zoned at eruption
- evolved from LSR-type compositions following extraction from mush roots

LSR: whole-rock <74 wt% SiO₂

- isolated bodies of crystal-poor rhyolite in the mush
- feedstock and compositional forerunner to the HSR melt-dominant body
- syn-eruptive exchange of melt and crystals with HSR
- some mixing with tholeiitic mafic magma

Biotite-bearing rhyolite

- 'foreign' magma, sourced from the nearby NE dome magma system
- syn-eruptively laterally fed into the initial Oruanui conduit
- syn-eruptive mixing-in of some HSR melt and crystals in the conduit

Tholeiitic mafic group

- extended interaction(s) with LSR-type material in the mush zone
- most macroscopic crystals inherited from LSR and/or HSR
- form three chemical subgroups depending on the timing and degree of interaction

Calc-alkaline mafic group

- less extensive interaction with rhyolites
- restricted compositional range
- most primitive melts with high-Ni, Fo₈₅ olivine

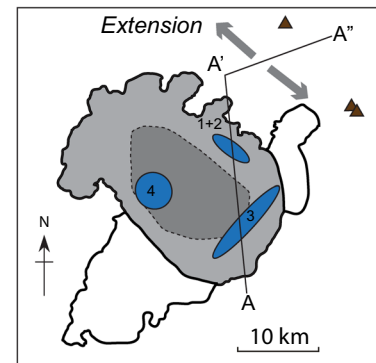


Fig. 16 Schematised scaled cross section through the Taupo area to show the sources, depths and pathways for the various crystal and melt components represented in the Oruanui eruption products

crystal mush body prior to their confluence in the melt-dominant magma body. Quartz crystals are inferred to have originated from an upper, cooler, SiO₂-saturated and highly evolved layer, whereas the majority of amphibole, orthopyroxene and plagioclase crystals largely originated from deeper, lesser evolved levels.

4. Origin of the LSR pumices. The LSR pumices were originally inferred by Wilson et al. (2006) to represent deeper and hotter parts of the melt dominant body. Here, these samples (as represented by individual pumices) are now interpreted to represent isolated bodies of crystal-poor rhyolite that were held within the crystal

mush and were tapped syn-eruptively (e.g. Cashman and Giordano 2014). In addition, the LSR melt (and entrained crystals) is recognised by us as having also previously been the feedstock material for the melt-dominant body. These conclusions are based on the distinct differences between the HSR and LSR glass chemistries (Fig. 2) and limited degrees of hybridisation in the pumices (i.e. minor melt and crystal exchanges between HSR and LSR, as inferred by Allan et al. 2013).

5. Wilson et al. (2006) suggested that the Oruanui mafic magmas, in particular the tholeiitic magma, had pon-

ded at the base of the melt-dominant magma body and initiated chamber-wide stirring and homogenisation. Subsequent work (Allan et al. 2013; Rooyakkers 2015; this paper) has shown that the mafic magmas were mostly interacting with the mush, as indicated by their accumulated felsic crystal populations and whole-rock trajectories trending towards LSR (rather than HSR) compositions (Figs. 12, 13). Commensurate with this revised interpretation, our data imply that vigorous convection was an inherent feature of the melt-dominant body from the moment of its inception, and not simply the result of late-stage introduction of mafic magmas.

Conclusions

The assembly and eruption of the Oruanui magma body was a complex, but geologically short lived, sequence of events. The work presented here and in other papers cited shows that there is a rich petrological record of these events in the compositions of melts and minerals, and in the textures of the mineral phases. The associated processes can be resolved into a cascade of events over timescales ranging from tens of thousands of years for the development of the deeper source mush zone to hundreds of seconds for the latest stages of magma rise before fragmentation and quenching. Key conclusions from the integration of previous and current Oruanui datasets are as follows.

1. Detailed compositional and textural records within Oruanui HSR quartz, plagioclase, orthopyroxene and amphibole crystals highlight the transition from compositional diversity in their early histories, to uniformity immediately prior to eruption. Melt extraction from the mush zone entrained crystals from all levels of the stratified crystal mush body, resulting in the juxtaposition of a diverse range of crystals within the melt-dominant magma body. A general outwards-cooling trend reflected in most mineral compositions show that the melt-dominant body cooled by ~40–50 °C during its lifetime and at that rate would have cooled back to mush within a few centuries to millennia had evacuation not occurred. Our data support the concept that eruptible magma bodies are very short lived when compared to the overall lifetime of the parental magmatic system (e.g. Glazner et al. 2004; Barboni and Schoene 2014; Barker et al. 2016).
2. The Oruanui mafic magmas record significant interactions with, or inheritance of, ‘rhyolite’ crystals (i.e. crystals with compositions appropriate for growth from rhyolite melts) from traversing through the mush zone during their eruption. Inheritance occurred over varying timescales, with reaction rims varying from only a few microns to >100 µm. However, ubiquitous down-temperature signals recorded in HSR crystals preclude the possibility that mafic magmas played any significant role in wholesale re-heating and/or re-mobilisation of the mush to cause eruption (cf. Bachmann and Dungan 2002; Huber et al. 2011; Barker et al. 2016). Syn-eruptive interactions between the mafic magmas and the melt-dominant magma body are recorded in zoned magnetite and olivine crystals, down to timescales of hours to tens of hours. Such short-term interactions can be directly linked with inferred eruptive timings and variations in the erupted proportions of mafic materials (Wilson 2001).
3. The disparate textural and compositional domains within single crystals, particularly HSR plagioclase and orthopyroxene, make complex the definitions of phenocrysts versus antecrysts for the Oruanui system. Despite the near-uniformity of rim compositions in the HSR crystals, the compositions and intensive parameters recorded by the crystal cores and interiors bear no direct relation to the melt-dominant body in which they were immersed at the time of eruption.
4. The magmatic systems giving rise to voluminous, crystal-poor rhyolites can be considered to operate in general on two contrasting timescales: longer term processes governing the broad compositional characteristics of the magma (i.e. fractional crystallisation, protolith assimilation, etc.) versus short-lived processes governing physical assembly of the melt-dominant magma body that actually erupts. The major crystallisation associated with the Oruanui magmatic system is represented by a dominant peak of zircon model ages centred on ~37–41 ka (Charlier et al. 2005; Wilson and Charlier 2009), in accord with the U/Th model age of bulk separates of the main crystal phases of 33 ka (+18/–16 ka: Charlier et al. 2005). Physical assembly of the melt-dominant magma body, as reflected in orthopyroxene zoning (Allan et al. 2013; this paper) and melt inclusion faceting (Pamukcu et al. 2015), occurred in <600 years, and mainly within the last ~100 years prior to eruption (i.e. 2–3 orders of magnitude faster than the processes of chemical evolution in the progenitor melts). On a global scale, such accumulation rates for eruptible magma are at the extreme, especially for such a large-sized eruption and appear to reflect the influence of tectonic processes acting on a mush system that held large quantities of melt. Only slightly smaller rates applied also to the youngest eruptions at Taupo (Barker et al. 2016). Both rate estimates are apparently orders of magnitude faster than those inferred for the comparably sized Bishop Tuff system (Chamberlain et al. 2014b; Simon et al. 2014).

5. The model inferred for the Oruanui magma system (extraction of melt plus some fraction of crystals from a crystal mush into a melt-dominant holding chamber) is similar to the model invoked for the Bishop Tuff (Hildreth and Wilson 2007; Chamberlain et al. 2015). Despite these broad similarities, the zonation characteristics of the deposits from these two eruptions are greatly different at whole-rock and single-crystal scales, reflecting different accumulation timescales for the respective melt-dominant bodies. The rapidity with which the Oruanui melt-dominant magma body accumulated, and the inferred rapid rates of heat loss, led to vigorous convection that destroyed any significant compositional and thermal zonation within the melt-dominant magma body prior to eruption.
6. The timescales inferred either for the lifetime of the overall Oruanui magmatic system or accumulation of its ~530 km³ melt-dominant magma body are much shorter than generalised estimates based on numerical modelling for similar sized magma bodies (e.g. Bachmann and Bergantz 2004; Annen 2009; Gelman et al. 2013; Caricchi et al. 2014b). The involvement of the mafic magmas and the rapid accumulation of the melt-dominant magma body are inferred to be the consequence of an enhanced episode of (magma-assisted) rifting in the crystal mush-bearing crust beneath Taupo during the lead into the Oruanui eruption. Following Rowland et al. (2010), we infer that tectonism associated with the rifted arc setting served to be a major (dominant?) control on (a) the rapidity of accumulation of the Oruanui melt-dominant body, (b) the fact that it grew to such a large size without prematurely evacuating, and (c) its consequent release on eruption in spasmodic fashion. Such a strong control by a non-volcanic factor raises questions as to how tectonic processes might have acted to control the development and eruption of other large caldera-related silicic systems.

Acknowledgements This work was supported by the Marsden Fund administered by the Royal Society of New Zealand (Grant VUW0813 to CJNW), a Bright Futures Top Achiever Doctoral Scholarship (for ASRA) administered by the Tertiary Education Commission of New Zealand, and Victoria University scholarships for SJB (PhD) and SMR (MSc). CJNW also acknowledges award of a James Cook Fellowship, administered by the Royal Society of New Zealand. We thank John Gamble, Jim Cole and Steve Blake for illuminating comments and discussions, and an anonymous reviewer, Michelle Coombs and, especially, Laura Waters for their comments.

References

- Allan ASR, Baker JA, Carter L, Wysoczanski RJ (2008) Reconstructing the quaternary evolution of the world's most active silicic volcanic system: insights from an ~1.65 Ma deep ocean tephra record sourced from Taupo Volcanic Zone, New Zealand. *Quat Sci Rev* 27:2341–2360
- Allan ASR, Wilson CJN, Millet M-A, Wysoczanski RJ (2012) The invisible hand: tectonic triggering and modulation of a rhyolitic supereruption. *Geology* 40:563–566
- Allan ASR, Morgan DJ, Wilson CJN, Millet M-A (2013) From mush to eruption in centuries: assembly of the super-sized Oruanui magma body. *Contrib Mineral Petrol* 166:143–164
- Annen C (2009) From plutons to magma chambers: thermal constraints on the accumulation of eruptible silicic magma in the upper crust. *Earth Planet Sci Lett* 284:409–416
- Aragon R, McCallister RH, Harrison HR (1984) Cation diffusion in titanomagnetites. *Contrib Mineral Petrol* 85:174–185
- Bachmann O, Bergantz GW (2004) On the origin of crystal-poor rhyolites: extracted from batholithic crystal mushes. *J Petrol* 45:1565–1582
- Bachmann O, Bergantz GW (2006) Gas percolation in upper-crustal silicic crystal mushes as a mechanism for upward heat advection and rejuvenation of near-solidus magma bodies. *J Volcanol Geotherm Res* 149:85–102
- Bachmann O, Bergantz GW (2008) Rhyolites and their source mushes across tectonic settings. *J Petrol* 49:2277–2285
- Bachmann O, Dungan MA (2002) Temperature-induced Al-zoning in hornblendes of the Fish Canyon magma, Colorado. *Am Mineral* 87:1062–1076
- Bachmann O, Huber C (2016) Silicic magma reservoirs in the Earth's crust. *Am Mineral* 101:2377–2404
- Bacon CR, Hirschmann MM (1988) Mg/Mn partitioning as a test for equilibrium between coexisting Fe–Ti oxides. *Am Mineral* 73:57–61
- Bacon CR, Lowenstern JB (2005) Late Pleistocene granodiorite source for recycled zircon and phenocrysts in rhyodacite lava at Crater Lake, Oregon. *Earth Planet Sci Lett* 233:277–293
- Bain AA, Jellinek AM, Wiebe RA (2013) Quantitative field constraints on the dynamics of silicic magma chamber rejuvenation and overturn. *Contrib Mineral Petrol* 165:1275–1294
- Barboni M, Schoene B (2014) Short eruption window revealed by absolute crystal growth rates in a granitic magma. *Nat Geosci* 7:524–528
- Barker SJ, Wilson CJN, Smith EGC, Charlier BLA, Wooden J, Hiess J, Ireland TR (2014) Post-supereruption magmatic reconstruction of Taupo volcano (New Zealand), as reflected in zircon ages and trace elements. *J Petrol* 55:1511–1533
- Barker SJ, Wilson CJN, Allan ASR, Schipper CI (2015) Fine-scale temporal recovery, reconstruction and evolution of a post-supereruption magmatic system: Taupo (New Zealand). *Contrib Mineral Petrol* 170:5
- Barker SJ, Wilson CJN, Morgan DJ, Rowland JV (2016) Rapid priming, accumulation and recharge of magma driving recent eruptions at a hyperactive caldera volcano. *Geology* 44:323–326
- Bégué F, Gualda GAR, Ghiorso MS, Pamukcu AS, Kennedy BM, Gravley DM, Deering CD, Chambefort I (2014) Phase-equilibrium geobarometers for silicic rocks based on rhyolite-MELTS. Part 2: application to Taupo Volcanic Zone rhyolites. *Contrib Mineral Petrol* 168:1082
- Bégué F, Gravley DM, Chambefort I, Deering CD, Kennedy BM (2015) Magmatic volatile distribution as recorded by rhyolitic melt inclusions in the Taupo Volcanic Zone, New Zealand. In: Zellmer GF, Edmonds M, Straub SM (eds) *The role of volatiles in the genesis, evolution and eruption of arc magmas*. Geological Society London Special Publications, vol 410, pp 71–94
- Blake S (1984) Volatile oversaturation during the evolution of silicic magma chambers as an eruption trigger. *J Geophys Res* 89:8237–8244

- Brey GP, Kohler T (1990) Geothermobarometry in 4-phase lherzolites 2. New thermobarometers, and practical assessment of existing thermobarometers. *J Petrol* 31:1353–1378
- Brophy JG (1991) Compositional gaps, critical crystallinity, and fractional crystallization in orogenic (calc-alkaline) magmatic systems. *Contrib Mineral Petrol* 109:173–182
- Brown SJA, Wilson CJN, Cole JW, Wooden J (1998) The Whakamaru group ignimbrites, Taupo Volcanic Zone, New Zealand: evidence for reverse tapping of a zoned silicic magma system. *J Volcanol Geotherm Res* 84:1–37
- Burgisser A, Bergantz GW (2011) A rapid mechanism to remobilize and homogenize highly crystalline magma bodies. *Nature* 471:212–217
- Caricchi L, Annen C, Blundy J, Simpson G, Pinel V (2014a) Frequency and magnitude of volcanic eruptions controlled by magma injection and buoyancy. *Nat Geosci* 7:126–130
- Caricchi L, Simpson G, Schaltegger U (2014b) Zircons reveal magma fluxes in the Earth's crust. *Nature* 511:457–461
- Cashman KV, Giordano G (2014) Calderas and magma reservoirs. *J Volcanol Geotherm Res* 288:28–45
- Cattell HJ, Cole JW, Oze C (2016) Volcanic and sedimentary facies of the Huka Group arc-basin sequence, Wairakei-Tauhara Geothermal Field, New Zealand. *NZ J Geol Geophys* 59:236–256
- Chamberlain KJ, Morgan DJ, Wilson CJN (2014a) Timescales of mixing and mobilisation in the Bishop Tuff magma body: perspectives from diffusion chronometry. *Contrib Mineral Petrol* 168:1034
- Chamberlain KJ, Wilson CJN, Wooden JL, Charlier BLA, Ireland TR (2014b) New perspectives on the Bishop Tuff from zircon textures, ages and trace elements. *J Petrol* 55:395–426
- Chamberlain KJ, Wilson CJN, Wallace PJ, Millet M-A (2015) Micro-analytical perspectives on the Bishop Tuff magma chamber. *J Petrol* 56:605–640
- Charlier BLA, Wilson CJN, Lowenstern JB, Blake S, van Calsteren PW, Davidson JP (2005) Magma generation at a large, hyperactive silicic volcano (Taupo, New Zealand) revealed by U–Th and U–Pb systematics in zircons. *J Petrol* 46:3–32
- Charlier BLA, Wilson CJN, Davidson JP (2008) Rapid open-system assembly of a large silicic magma body: time-resolved evidence from cored plagioclase crystals in the Oruanui eruption deposits, New Zealand. *Contrib Mineral Petrol* 156:799–813
- Charlier BLA, Wilson CJN, Mortimer N (2010) Evidence from zircon U–Pb age spectra for crustal structure and felsic magma genesis at Taupo volcano, New Zealand. *Geology* 38:915–918
- Charlier BLA, Morgan DJ, Wilson CJN, Wooden JL, Allan ASR, Baker JA (2012) Lithium concentration gradients in feldspar and quartz record the final minutes of magma ascent in an explosive supereruption. *Earth Planet Sci Lett* 319–320:218–227
- Coombs ML, Gardner JE (2004) Reaction rim growth on olivine in silicic melts: implications for magma mixing. *Am Mineral* 89:748–759
- Coombs ML, Eichelberger JC, Rutherford MJ (2000) Magma storage and mixing conditions for the 1953–1974 eruptions of Southwest Trident volcano, Katmai National Park, Alaska. *Contrib Mineral Petrol* 140:99–118
- Costa F, Dohmen R, Chakraborty S (2008) Timescales of magmatic processes from modelling the zoning patterns of crystals. In: Putirka KD, Tepley FJ (eds) *Minerals, inclusions and volcanic processes*. Reviews in Mineralogy and Geochemistry, vol 69, pp 545–594
- Davidson JP, Hora JM, Garrison JM, Dungan MA (2005) Crustal forensics in arc magmas. *J Volcanol Geotherm Res* 140:157–170
- de Silva SL, Gregg PM (2014) Thermomechanical feedbacks in magmatic systems: implications for growth, longevity, and evolution of large caldera-forming magma reservoirs and their supereruptions. *J Volcanol Geotherm Res* 282:77–91
- Devine JD, Rutherford MJ, Norton GE, Young SR (2003) Magma storage region processes inferred from geochemistry of Fe–Ti oxides in andesitic magma, Soufrière Hills Volcano, Montserrat, WI. *J Petrol* 44:1375–1400
- Dohmen R, Ter Heege JH, Becker H-W, Chakraborty S (2016) Fe–Mg interdiffusion in orthopyroxene. *Am Mineral* 101:2210–2221
- Dungan MA, Davidson J (2004) Partial assimilative recycling of the mafic plutonic roots of arc volcanoes: an example from the Chilean Andes. *Geology* 32:773–776
- Eichelberger JC (1978) Andesitic volcanism and crustal evolution. *Nature* 275:21–27
- Evans BW, Bachmann O (2013) Implications of equilibrium and disequilibrium among crystal phases in the Bishop Tuff. *Am Mineral* 98:271–274
- Evans BW, Scaillet B, Keuhner SK (2006) Experimental determination of coexisting iron–titanium oxides in the systems FeTiAlO, FeTiAlMgO, FeTiAlMnO, and FeTiAlMgMnO at 800 and 900 °C, 1–4 kbar, and relatively high oxygen fugacity. *Contrib Mineral Petrol* 152:149–167
- Evans BW, Hildreth W, Bachmann O, Scaillet B (2016) In defence of magnetite-ilmenite thermometry in the Bishop Tuff and its implication for gradients in silicic magma reservoirs. *Am Mineral* 101:469–482
- Ewart A, Stipp JJ (1968) Petrogenesis of the volcanic rocks of the central North Island, New Zealand, as indicated by a study of Sr⁸⁷/Sr⁸⁶ ratios, and Sr, Rb, K, U and Th abundances. *Geochim Cosmochim Acta* 32:699–736
- Foroozan R, Elsworth D, Voight B, Mattioli GS (2011) Magmatic-metering controls the stopping and restarting of eruptions. *Geophys Res Lett* 38:L05306
- Freer R, Hauptman Z (1978) Experimental study of magnetite-titanomagnetite interdiffusion. *Phys Earth Planet Int* 16:223–231
- Gamble JA, Wood CP, Price RC, Smith IEM, Stewart RB, Waight T (1999) A fifty year perspective of magmatic evolution on Ruapehu Volcano, New Zealand: verification of open system behaviour in an arc volcano. *Earth Planet Sci Lett* 170:301–314
- Gelman SE, Gutierrez FJ, Bachmann O (2013) On the longevity of large upper crustal silicic magma reservoirs. *Geology* 41:759–762
- Ghiorso MS, Evans BW (2008) Thermodynamics of rhombohedral oxide solid solutions and a revision of the Fe–Ti two-oxide geothermometer and oxygen-barometer. *Am J Sci* 308:957–1039
- Girard G, Stix J (2010) Rapid extraction of discrete magma batches from a large differentiating magma chamber: the Central Plateau Member rhyolites, Yellowstone caldera, Wyoming. *Contrib Mineral Petrol* 160:441–465
- Glazner AF, Bartley JM, Coleman DS, Gray W, Taylor RZ (2004) Are plutons assembled over millions of years by amalgamation from small magma chambers? *GSA Today* 14(4/5):4–11
- Gregg PM, de Silva SL, Grosfils EB, Parmigiani JP (2012) Catastrophic caldera-forming eruptions: thermomechanics and implications for eruption triggering and maximum caldera dimensions on Earth. *J Volcanol Geotherm Res* 241–242:1–12
- Gualda GAR, Sutton SR (2016) The year leading to a supereruption. *PLoS One* 11:e0159200
- Gualda GAR, Pamukcu AS, Ghiorso MS, Anderson AT, Sutton SR, Rivers ML (2012a) Timescales of quartz crystallization and the longevity of the Bishop giant magma body. *PLoS One* 7:e37492
- Gualda GAR, Ghiorso MS, Lemons RV, Carley TL (2012b) Rhyolite-MELTS: a modified calibration of MELTS optimized for silica-rich, fluid-bearing magmatic systems. *J Petrol* 53:875–890

- Hammond PA, Taylor LA (1982) The ilmenite/titano-magnetite assemblage: kinetics of re-equilibration. *Earth Planet Sci Lett* 61:143–150
- Hellstrom J, Paton C, Woodhead JD, Hergt JM (2008) Iolite: software for spatially resolved LA-(quad and MC) ICPMS analysis. In: Sylvester, P (ed) *Laser ablation ICP-MS in the earth sciences: current practices and outstanding issues*. Mineralogical Association of Canada short course series, vol 40, pp 343–348
- Hildreth W (1979) The Bishop Tuff: evidence for the origin of compositional zonation in silicic magma chambers. In: Chapin CE, Elston WE (eds) *Ash-flow tuffs*. Geological Society of America Special Papers, vol 180, pp 43–75
- Hildreth W (2004) Volcanological perspectives on Long Valley, Mammoth Mountain, and Mono Craters: several contiguous but discrete systems. *J Volcanol Geotherm Res* 136:169–198
- Hildreth W, Wilson CJN (2007) Compositional zoning of the Bishop Tuff. *J Petrol* 48:951–999
- Housh TB, Luhr JF (1991) Plagioclase-melt equilibria in hydrous systems. *Am Mineral* 76:477–492
- Huang R, Audétat A (2012) The titanium-in-quartz (TitaniQ) thermometer: a critical examination and re-calibration. *Geochim Cosmochim Acta* 84:75–89
- Huber C, Bachmann O, Manga M (2010) Two competing effects of volatiles on heat transfer in crystal-rich magmas: thermal insulation vs defrosting. *J Petrol* 51:847–867
- Huber C, Bachmann O, Dufek J (2011) Thermo-mechanical reactivation of locked crystal mushes: melting-induced internal fracturing and assimilation processes in magmas. *Earth Planet Sci Lett* 304:443–454
- Huber C, Bachmann O, Dufek J (2012) Crystal-poor versus crystal-rich ignimbrites: a competition between stirring and reactivation. *Geology* 40:115–118
- Jellinek AM, DePaolo DJ (2003) A model for the origin of large silicic magma chambers: precursors of caldera-forming eruptions. *Bull Volcanol* 65:363–381
- Kaneko K, Inoue K, Koyaguchi T, Yoshikawa M, Shibata T, Takahashi T, Furukawa K (2015) Magma plumbing system of the Aso-3 large pyroclastic eruption cycle at Aso volcano, Southwest Japan: petrological constraint on the formation of a compositionally stratified magma chamber. *J Volcanol Geotherm Res* 303:41–58
- Karlstrom L, Rudolph ML, Manga M (2012) Caldera size modulated by the yield stress within a crystal-rich magma reservoir. *Nat Geosci* 5:402–405
- Langridge RM, Ries W, Litchfield NJ, Villamor P, Van Dissen RJ, Barrell DJA, Rattenbury MS, Heron DW, Haubrock S, Townsend DB, Lee JM, Berryman KR, Nicol A, Cox SC, Stirling MW (2016) The New Zealand active faults database. *NZ J Geol Geophys* 59:86–96
- Leonard GS, Cole JW, Nairn IA, Self S (2002) Basalt triggering of the c. AD 1305 Kaharoa rhyolite eruption, Tarawera Volcanic Complex, New Zealand. *J Volcanol Geotherm Res* 115:461–486
- Leonard GS, Begg JG, Wilson CJN (2010) Geology of the Rotorua area. Institute of Geological and Nuclear Sciences 1:250,000 geological map 5. Institute of Geological and Nuclear Sciences, Lower Hutt
- Lipman PW (1997) Subsidence of ash-flow calderas: relation to caldera size and magma-chamber geometry. *Bull Volcanol* 59:198–218
- Liu Y, Anderson AT, Wilson CJN, Davis AM, Steele IM (2006) Mixing and differentiation in the Oruanui rhyolitic magma, Taupo, New Zealand: evidence from volatiles and trace elements in melt inclusions. *Contrib Mineral Petrol* 151:71–87
- Liu Y, Anderson AT, Wilson CJN (2007) Melt pockets in phenocrysts and ascent rates of silicic magmas. *J Geophys Res* 112:B06204
- Lowe DJ, Shane PAR, Alloway BV, Newnham RM (2008) Fingerprints and age models for widespread New Zealand tephra marker beds erupted since 30,000 years ago: a framework for NZ-INTIMATE. *Quat Sci Rev* 27:95–126
- Lowe DJ, Blaauw M, Hogg AG, Newnham RM (2013) Ages of 24 widespread tephra erupted since 30,000 years ago in New Zealand, with re-evaluation of the timing and palaeoclimatic implications of the Lateglacial cool episode recorded at Kaipo bog. *Quat Sci Rev* 74:170–194
- Malfait W, Seifert R, Petitgirard S, Perrillat J-P, Mezouar M, Ota T, Nakamura E, Lerch P, Sanchez-Valle C (2014) Supervolcano eruptions driven by melt buoyancy in large silicic chambers. *Nat Geosci* 7:122–125
- Martin VM, Morgan DJ, Jerram DA, Caddick MJ, Prior DJ, Davidson JP (2008) Bang! month-scale eruption triggering at Santorini Volcano. *Science* 321:1178
- Matthews NE, Pyle DM, Smith VC, Wilson CJN, Huber C, van Hinsberg V (2012) Quartz zoning and the pre-eruptive evolution of the ~340-ka Whakamaru magma systems, New Zealand. *Contrib Mineral Petrol* 163:87–107
- Miyashiro A (1974) Volcanic rock series in island arcs and active continental margins. *Am J Sci* 274:321–355
- Moore G, Vennemann T, Carmichael ISE (1998) An empirical model for the solubility of H₂O in magmas to 3 kilobars. *Am Mineral* 83:36–42
- Myers ML, Wallace PJ, Wilson CJN, Morter BK, Swallow EJ (2016) Prolonged ascent and episodic venting of discrete magma batches at the onset of the Huckleberry Ridge supereruption, Yellowstone. *Earth Planet Sci Lett* 451:285–297
- Nakamura M (1995) Continuous mixing of crystal mush and replenished magma in the ongoing Unzen eruption. *Geology* 23:807–810
- Nelson ST, Montana A (1992) Sieve-textured plagioclase in volcanic rocks produced by rapid decompression. *Am Mineral* 77:1242–1249
- Pallister JS, Hoblitt RP, Reyes AG (1992) A basalt trigger for the 1991 eruptions of Pinatubo volcano. *Nature* 356:426–428
- Pamukcu AS, Gualda GAR, Anderson AT (2012) Crystallization stages of the Bishop Tuff magma body recorded in crystal textures in pumice clasts. *J Petrol* 53:589–609
- Pamukcu AS, Gualda GAR, Bégué F, Gravelly DM (2015) Melt inclusion shapes: timekeepers of short-lived giant magma bodies. *Geology* 43:947–950
- Pamukcu AS, Ghiorsio MS, Gualda GAR (2016) High-Ti, bright-CL rims in volcanic quartz: a result of very rapid growth. *Contrib Mineral Petrol* 171:105
- Parmigiani A, Huber C, Bachmann O (2014) Mush microphysics and the reactivation of crystal-rich magma reservoirs. *J Geophys Res: Solid Earth* 119:6308–6322
- Pearce NJG, Westgate JA, Perkins WT (1996) Developments in the analysis of volcanic glass shards by laser ablation ICP-MS: quantitative and single internal standard multi-element methods. *Quat Int* 34–36:213–227
- Peppard BT, Steele IM, Davis AM, Wallace PJ, Anderson AT (2001) Zoned quartz phenocrysts from the rhyolitic Bishop Tuff. *Am Mineral* 86:1034–1052
- Price RC, Mortimer N, Smith IEM, Maas R (2015) Whole-rock geochemical reference data for Torlesse and Waipapa terranes, North Island, New Zealand. *NZ J Geol Geophys* 58:213–228
- Putirka KD (2008) Thermometers and barometers for volcanic systems. In: Putirka KD, Tepley FJ (eds) *Minerals, inclusions and*

- volcanic processes. *Reviews in Mineralogy and Geochemistry*, vol 69, pp 61–120
- Reid MR (2008) How long does it take to supersize an eruption? *Elements* 4:23–28
- Reid MR, Vazquez JA, Schmitt AK (2011) Zircon-scale insights into the history of a supervolcano, Bishop Tuff, Long Valley, California, with implications for the Ti-in-zircon geothermometer. *Contrib Mineral Petrol* 161:293–311
- Ridolfi F, Renzulli A, Puerini M (2010) Stability and chemical equilibrium of amphibole in calc-alkaline magmas: an overview, new thermobarometric formulations and application to subduction-related volcanoes. *Contrib Mineral Petrol* 160:45–66
- Rooyackers SM (2015) A textural and micro-analytical study of quenched mafic inclusions from the Oruanui eruption, Taupo volcano, New Zealand. MSc thesis, Victoria University of Wellington
- Rowland JV, Wilson CJN, Gravley DM (2010) Spatial and temporal variations in magma-assisted rifting, Taupo Volcanic Zone, New Zealand. *J Volcanol Geotherm Res* 190:89–108
- Sauerzapf U, Lattard D, Burchard M, Engelman R (2008) The titanomagnetite-ilmenite equilibrium: new experimental data and thermo-oxybarometric application to the crystallization of basic to intermediate rocks. *J Petrol* 49:1161–1185
- Self S (1983) Large-scale phreatomagmatic silicic volcanism: a case study from New Zealand. *J Volcanol Geotherm Res* 17:433–469
- Self S (2006) The effects and consequences of very large explosive volcanic eruptions. *Philos Trans R Soc Lond A364*:2073–2097
- Self S, Sparks RSJ (1978) Characteristics of widespread pyroclastic deposits formed by the interaction of silicic magma and water. *Bull Volcanol* 41:196–212
- Shaw HR (1985) Links between magma-tectonic rate balances, plutonism, and volcanism. *J Geophys Res* 90:11275–11288
- Simon JL, Weis D, DePaolo DJ, Renne PR, Mundil R, Schmitt AK (2014) Assimilation of preexisting Pleistocene intrusions at Long Valley by periodic magma recharge accelerates rhyolite generation: rethinking the melting model. *Contrib Mineral Petrol* 167:955
- Smith RL (1979) Ash-flow magmatism. In: Chapin CE, Elston WE (eds) *Ash-flow Tuffs*. Geological Society of America Special Papers, vol 180, pp 5–27
- Snyder D (2000) Thermal effects of the intrusion of basaltic magma into a more silicic magma chamber and implications for eruption triggering. *Earth Planet Sci Lett* 175:257–273
- Sparks RSJ, Sigurdsson H, Wilson L (1977) Magma mixing: a mechanism for triggering acid explosive eruptions. *Nature* 267:315–318
- Sparks RSJ, Huppert HE, Turner JS (1984) The fluid dynamics of evolving magma chambers. *Philos Trans R Soc Lond A310*:511–534
- Sutton AN (1995) Evolution of a large silicic magma system: Taupo volcanic centre, New Zealand. Unpubl PhD thesis, The Open University, Milton Keynes, UK
- Sutton AN, Blake S, Wilson CJN (1995) An outline geochemistry of rhyolite eruptives from Taupo volcanic centre, New Zealand. *J Volcanol Geotherm Res* 68:153–175
- Thomas JB, Watson EB, Spear FS, Shemella PT, Nayak SK, Lanzirrotti A (2010) TitaniQ under pressure: the effect of pressure and temperature on the solubility of Ti in quartz. *Contrib Mineral Petrol* 160:743–759
- Thomas JB, Watson EB, Spear FS, Wark DA (2015) TitaniQ recrystallized: experimental confirmation of the original Ti-in-quartz calibrations. *Contrib Mineral Petrol* 169:27
- Tsuyuhama A (1985) Dissolution kinetics of plagioclase in the melt of the system diopside-albite-anorthite, and origin of dusty plagioclase in andesites. *Contrib Mineral Petrol* 89:1–16
- Van Eaton AR, Wilson CJN (2013) The nature, origins and distribution of ash aggregates in a large-scale wet eruption deposit: Oruanui, New Zealand. *J Volcanol Geotherm Res* 250:129–154
- Van Eaton AR, Herzog M, Wilson CJN, McGregor J (2012) Ascent dynamics of large phreatomagmatic eruption clouds: the role of microphysics. *J Geophys Res* 117:B03203
- Vandergoes MJ, Hogg AG, Lowe DJ, Newnham RM, Denton GH, Southon J, Barrell DJA, Wilson CJN, McGlone MS, Allan ASR, Almond PC, Petchey F, Dabell K, Dieffenbacher-Krall AC, Blaauw M (2013) A revised age for the Kawakawa/Oruanui Tephra, a key marker for the last glacial maximum in New Zealand. *Quat Sci Rev* 74:195–201
- Venezky DY, Rutherford MJ (1999) Petrology and Fe–Ti oxide reequilibration of the 1991 Mount Unzen mixed magma. *J Volcanol Geotherm Res* 89:213–230
- Wark DA, Watson EB (2006) TitaniQ: a titanium-in-quartz geothermometer. *Contrib Mineral Petrol* 152:743–754
- Wark DA, Hildreth W, Spear FS, Cherniak DJ, Watson EB (2007) Pre-eruption recharge of the Bishop magma system. *Geology* 35:235–238
- Waters LE, Lange RA (2015) An updated calibration of the plagioclase-liquid hygrometer-thermometer applicable to basalts through rhyolites. *Am Mineral* 100:2172–2184
- Wilson CJN (2001) The 26.5 ka Oruanui eruption, New Zealand: an introduction and overview. *J Volcanol Geotherm Res* 112:133–174
- Wilson CJN, Charlier BLA (2009) Rapid rates of magma generation at contemporaneous magma systems, Taupo volcano, New Zealand: insights from U–Th model-age spectra in zircons. *J Petrol* 50:875–907
- Wilson CJN, Blake S, Charlier BLA, Sutton AN (2006) The 26.5 ka Oruanui eruption, Taupo volcano, New Zealand: development, characteristics and evacuation of a large rhyolitic magma body. *J Petrol* 47:35–69
- Wilson CJN, Gravley DM, Leonard GS, Rowland JV (2009) Volcanism in the central Taupo Volcanic Zone, New Zealand: tempo, styles and controls. In: Thordarson T, Self S, Larsen G, Rowland SK, Hoskuldsson A (ed) *Studies in volcanology: the legacy of George Walker*. Special Publications of IAVCEI, vol 2, pp 225–247
- Wilson CJN, Seward TM, Charlier BLA, Allan ASR, Bello L (2012) A comment on: ‘TitaniQ under pressure: the effect of pressure and temperature on the solubility of Ti in quartz’, by Jay B. Thomas, E. Bruce Watson, Frank S. Spear, Philip T. Shemella, Saroj K. Nayak and Antonio Lanzirrotti. *Contrib Mineral Petrol* 164:359–368
- Wotzlaw J-F, Bindeman IN, Stern RA, D’Abzac F-X, Schaltegger U (2015) Rapid heterogeneous assembly of multiple magma reservoirs prior to Yellowstone supereruptions. *Sci Rep* 5:srep14026